Monthly Notices of the ROYAL ASTRONOMICAL SOCIETY
MNRAS **480,** 629–651 (2018) doi:10.1093/mnras/sty1840
Advance Access publication 2018 July 19

Surface brightness fluctuation spectrum: a new probe of evolved stars in unresolved stellar populations

Martin Mitzkus,[1★] C. Jakob Walcher,[1★] Martin M. Roth,[1] Paula R. T. Coelho,[2] Maria-Rosa L. Cioni,[1] Gabriella Raimondo[3] and Marina Rejkuba[4]

[1]*Leibniz-Institut für Astrophysik Potsdam (AIP), An der Sternwarte 16, D-14482 Potsdam, Germany*
[2]*Instituto de Astronomia, Geofísica e Ciências Atmosféricas, Universidade de São Paulo, R. do Matão 1226, 05508-090 São Paulo, Brazil*
[3]*INAF-Osservatorio Astronomico d'Abruzzo, Via Mentore Maggini s.n.c., I-64100 Teramo, Italy*
[4]*European Southern Observatory, Karl-Schwarzschild-Straße 2, D-85748 Garching bei München, Germany*

Accepted 2018 July 6. Received 2018 July 02; in original form 2018 February 23

ABSTRACT

The surface brightness fluctuation (SBF) method measures spatial fluctuations due to the most luminous stars in a galaxy. Besides being useful for distance measurements, it also provides diagnostic power to investigate the contribution of the brightest stars to the underlying unresolved stellar population. We apply the SBF technique to every wavelength layer in integral field spectroscopy data obtained with the MUSE instrument. This yields the first SBF spectrum of a galaxy. SBF spectra combine the sensitivity of SBF to luminous stars with the physical information content of spectra. We show that the SBF spectrum of the S0 galaxy NGC 5102 is dominated by spectra of M-type giants (red giant branch, asymptotic giant branch, and red supergiant stars). We build the first stellar population synthesis tool that predicts SBF spectra. Through comparison of integrated spectra from our new tool with published model spectra, we confirm that it is mathematically correct. We use the integrated spectrum and a bootstrap method to derive an ensemble of (degenerate) star formation histories of NGC 5102. We compute a model SBF spectrum for each star formation history. Given that some models do not reproduce the observed SBF spectrum well, we are able to obtain additional constraints on the star formation history, leading to marginally reduced uncertainties on the mean age and metallicity. This result is confirmed by modelling mock spectra with different star formation histories.

Key words: methods: data analysis – galaxies: elliptical and lenticular, cD – galaxies: individual: NGC 5102 – galaxies: stellar content.

1 INTRODUCTION

Surface brightness fluctuations (SBFs) measure the spatial brightness variations in a galaxy image introduced by the random sampling of the stellar population in every resolution element (pixel). This technique had been used for some time in radio astronomy (Scheuer 1957) and was introduced 30 years ago in optical astronomy as a tool to measure (extragalactic) distances by Tonry & Schneider (1988). Nowadays, the SBF method is one of the most precise distance indicators available for early-type galaxies out to 100 Mpc with near-infrared (e.g. Jensen et al. 2001, 2015) and optical (Biscardi et al. 2008; Blakeslee et al. 2009) observations at space-based image resolution.

By definition, SBFs are sensitive to the most luminous stars in a stellar population. In turn this means that SBFs depend on the properties of the underlying stellar population. Which evolutionary phase is brightest and hence manifested in the SBF depends not only on the wavelength range (i.e. photometric band) but also on the age of the stellar population (e.g. Liu, Charlot & Graham 2000; Cantiello et al. 2003). For intermediate to old stellar populations, the SBF signal in the optical and especially in the infrared is dominated by red giant branch (RGB) and asymptotic giant branch (AGB) stars. The initial results showed that SBF magnitudes correlate with colour (e.g. Tonry 1991; Sodemann & Thomsen 1996) and that SBF magnitudes and colours are metallicity dependent (Ajhar & Tonry 1994). This is due to the temperature sensitivity of the giant branch, which leads to temperature-sensitive SBF (e.g. Worthey 1993).

The evolution of stars in some evolutionary phases and mass ranges is not always well understood, e.g. massive stars, Wolf–Rayet stars, red supergiants, and thermally pulsating AGB (TP-AGB) stars. In particular, the TP-AGB evolutionary phase is short and complex (for a review see Herwig 2005).

★ E-mail: mmitzkus@aip.de (MM); jwalcher@aip.de (CJW)

Published by Oxford University Press on behalf of the Royal Astronomical Society

Even though TP-AGB stars are short-lived, they are extremely luminous and therefore important for the interpretation of the light of unresolved stellar populations (e.g. Maraston 2005; Conroy, Gunn & White 2009). TP-AGB stars affect both optical and infrared regions of stellar population models. Because of the complexity of the physical processes at work in this kind of stars and the difficulties to constrain them, stellar population synthesis models typically do not match well, at the same time, optical and infrared wavelength ranges (Eminian et al. 2008; Zibetti, Charlot & Rix 2009; Taylor et al. 2011).

It is the sensitivity of SBF to AGB stars that has led Cantiello et al. (2003) to use SBF to constrain AGB mass loss. Subsequently, Raimondo et al. (2005) and Raimondo (2009) have confirmed that SBF magnitudes are sensitive to AGB mass loss rates. In contrast to these findings, González-Lópezlira et al. (2010) have found only weak or no dependence of SBF magnitudes on AGB mass loss.

Constraining stellar population models using SBF magnitudes is a difficult task because they depend on distance, and also on population age and metallicity, which is why SBF may also be used as an effective probe of unresolved stellar population properties. The use of SBF colours partly overcomes the problem (e.g. Cantiello et al. 2007). Moreover, in comparison with galaxy data, we are faced with the fact that SBF predictions are mostly based on single-age, single-metallicity population (SSP) models, while galaxies certainly contain composite stellar populations. The minimum requirement that the models have to fulfill is that they cover the same parameter space in a diagnostic diagram as the data (i.e. colour versus SBF magnitude or colour versus SBF colour). Liu, Graham & Charlot (2002) have shown that contradicting models can still span the range of observed galaxy properties. The model uncertainties in the TP-AGB modelling of infrared SBF have been highlighted in Jensen et al. (2015). Even though the differences between models are sometimes drastic (see figs 7 and 8 in Jensen et al. 2015), it is hard to say which model performs better on the basis of SBF magnitudes and colours in just a few bands.

In this paper, we introduce a new application of the SBF technique based on the spectrally resolved SBF to obtain the galaxy *SBF spectrum*. To meet this goal, integral field spectroscopy (IFS) over a sufficiently large field of view and with a sufficient spatial sampling is needed. The only instrument that is currently fulfilling such requirements is the new second generation instrument 'Multi Unit Spectroscopic Explorer' (MUSE, Bacon et al. 2010) mounted at the ESO Very Large Telescope. We apply the classical SBF technique to several thousand pseudo-images of integral spectrograph data to obtain the SBF spectrum from 4800 to 9300 Å with a sampling of 1.25 Å and a spectral resolution of 2.5 Å.

The SBF spectra combine the sensitivity to the brightest stars in a stellar population with the physical information content spectra provide by resolving absorption and emission lines. So we expect that only SBF *spectra* can reveal the full power of SBF for population studies and will be much better suited to constrain models than photometry.

Our approach of resolving the SBF spectrally should not be confused with the 'fluctuation spectroscopy' (FS) of van Dokkum & Conroy (2014). The FS approach is methodically different from our approach: We adopt for the first time the SBF technique of Tonry & Schneider (1988) and apply it to IFS data. FS measures instead the response of spectral indices to the relative broad-band brightness of pixels. In essence SBF spectra amplify the signal from giant stars (we call this the 'diagnostic power' of SBF) while FS measures the response of the indices (or equivalently the spectrum) to the fraction of giant stars. van Dokkum & Conroy (2014) apply the FS to six narrow-band images; however, the method can be applied to IFS data as well. SBF spectra and FS are two complementary approaches for probing giant stars in unresolved stellar populations.

In Section 2 we describe the target selection and summarize the properties of NGC 5102, the observations, and the data reduction. The extraction of the SBF spectrum from the IFS data cube is detailed in Section 3. A comparison of the SBF spectrum to stellar spectra of spectral types M is presented in Section 4. As a supplement to this section, we search for spectral features of C-stars in the SBF spectrum in Appendix A. In order to compare the SBF spectrum to stellar population models, we constructed a population synthesis model that predicts SBF spectra (Section 5) and use these models in Section 6 to fit the star formation history (SFH) and compare it with the SBF spectrum.

2 DATA

2.1 Observations and data reduction

For this pilot study on the feasibility of measuring SBF from MUSE data, we selected a galaxy that is well suited for SBF measurement: NGC 5120 is the galaxy with the brightest apparent SBF magnitude from the SBF *I*-band survey (Tonry et al. 1997, 2001) that is visible from Paranal Observatory in June ($200^\circ \leq$ RA $\leq 340^\circ$ and Dec. $\leq -10^\circ$).

NGC 5102 was observed during the MUSE science verification run [programme 60.A-9308(A), PI: Mitzkus] during the night of 2014 June 23 to 24. MUSE is a panoramic IFS instrument with a 60×60 arcsec field of view and 0.2 arcsec spatial sampling (assuming a distance of 4 Mpc to NGC 5102, this corresponds to a physical scale of 3.9 pc per pixel; see Section 2.3). The wavelength coverage is nominally from 4800 to 9300 Å. We obtained four object exposures of 960 s each, rotated by 90° to distribute the residuals of the image-slicer system homogeneously over the field of view. The data reduction was carried out with the dedicated MUSE data reduction software (Weilbacher et al. 2012) version 1.0.1, following the standard procedure. In order to keep pixel interpolations to a minimum, the MUSE data reduction software reduces the data in a pixtable format, where for every CCD pixel the flux, CCD position, wavelength, and spatial position are stored. The final step is a drizzling of the pixtable data to the output data cube, following the Fruchter et al. (2009) drizzle strategy, however in a 3D version. The final product is a cube with a mean signal -to-noise ratio (SNR) per volume pixel of 4.5 and a spatial full width at half-maximum (FWHM) of 0.7 arcsec. The data set and the reduction have been described in detail in Mitzkus, Cappellari & Walcher (2017).

2.2 Correcting the radial velocity shifts

SBF measure the intrinsic surface brightness variance over the face of a galaxy that arises due to the random distribution of stars. So far the SBF method has been applied only to imaging data, sometimes in multiple bands. In our new approach, we have measured the SBF in thousands of spectrally resolved images (layers) of MUSE data cubes, with a spectral resolution that is orders of magnitude better than for imaging data (2.5 Å spectral resolution of MUSE compared to a FWHM of about 1000 Å for typical broad-band filters in the optical). This in turn has implications for the data reduction and the SBF analysis. To measure a meaningful SBF spectrum, it is required that one wavelength layer of the data cube represent one rest-frame wavelength. A spatially varying redshift (as is typically caused by the rotation of a galaxy) will smear out spectral features, e.g. an absorption line, over several wavelength layers of the data cube. Therefore, we have to correct the spectra for the line-of-sight velocity v individually for each spatial resolution element.

Mitzkus et al. (2017) have measured the velocity field of NGC 5102 from the same data set (see their fig. 2) and it was used here to shift all spectra to the same rest-frame velocity. The line-of-sight velocity has been measured on spatially binned spectra using the Voronoi tessellation algorithm of Cappellari & Copin (2003) to ensure a homogeneous and sufficiently high SNR for an unbiased measurement of the kinematics (for the details we refer to Mitzkus et al. 2017).

The fact that SBFs measure the intrinsic brightness differences between neighbouring pixels means that during the data reduction interpolations should be kept to a minimum (Mei et al. 2005). Any interpolation will correlate the fluxes of neighbouring pixels and thus reduce the SBF signal. It will also cause correlations in the noise between pixels, leading to a noise power spectrum that is tilted, not flat. Fortunately the MUSE data reduction software interpolates the data only once, i.e. in the final step where the data cube is produced. All previous data reduction steps are applied to the data in the pixtable format.

Correcting the radial velocity shifts in the final data cube would result in a second pixel interpolation. In order to avoid this second interpolation, we corrected the radial velocities in the pixtables, after combining the fully reduced individual exposures, but before producing the final data cube. For every CCD pixel, we computed the corrected wavelength from the velocity of the spatially nearest Voronoi bin (in RA and Dec. of the centre position of the Voronoi bin). The final data cube was computed from this radial velocity corrected pixtable using the standard MUSE data reduction tool.

2.3 NGC 5102

The Centaurus group galaxy NGC 5102 is a low-luminosity S0 galaxy (Karachentsev et al. 2002). The SBF distance to NGC 5102 was measured to be 4.0 ± 0.2 Mpc by Tonry et al. (2001). Other distance estimators find slightly smaller distances: The planetary nebula luminosity function distance was measured as 3.1 Mpc (McMillan, Ciardullo & Jacoby 1994) and the tip of the red giant branch measurement scatter between 3.2 (Davidge 2008) and 3.74 Mpc (Tully et al. 2015). The stellar mass of NGC 5102 has been estimated to be $(5.6 \pm 0.8) \times 10^9$ M$_\odot$ (Beaulieu et al. 2010), broadly consistent with the estimate from Davidge (2015).

While the photometric appearance of NGC 5102 is like that of a typical S0 galaxy (Pritchet 1979; Davidge 2015), this galaxy has a number of peculiarities. Freeman was the first one to notice the unusually blue colour of the nucleus (Eggen 1971) that was later attributed to the presence of a star cluster with an age of $\sim 10^8$ yr (e.g. Gallagher, Faber & Balick 1975; van den Bergh 1976; Pritchet 1979). Also the 3.3×10^8 M$_\odot$ H I reservoir (Gallagher et al. 1975) is relatively large for S0 galaxies. The H I is distributed in a ring-like structure with a radius of 2.2 kpc and a prominent central depression (van Woerden et al. 1993). van den Bergh (1976) has detected an H α emission structure that was later also seen in [O III] (McMillan et al. 1994). The ring-like structure and the fact that the emission line ratios indicate shock ionization lead to the conclusion that this is a supershell (McMillan et al. 1994). Based on the velocity of the gas and the size of the ring, these authors estimate an age of about 10^7 years for the supershell.

Mitzkus et al. (2017) have found that NGC 5102 is a 2σ galaxy (Krajnović et al. 2011), composed of two counterrotating stellar discs. The more centrally concentrated disc corotates with the H I gas (van Woerden et al. 1993; Kamphuis et al. 2015; Mitzkus et al. 2017).

The stellar population in NGC 5102 has been investigated by several authors. In the centre, Beaulieu et al. (2010) have measured a constant star formation rate over the last 0.2 Gyr and a burst about 20 Myr ago, in agreement with Deharveng et al. (1997). This burst is in remarkable agreement with the estimated age of the supershell. Davidge (2015) has derived a luminosity-weighted SSP age for the nucleus of $1^{+0.2}_{-0.1}$ Gyr and for the bulge of $2^{+0.5}_{-0.2}$ Gyr. The first IFS-based, i.e. spatially resolved, investigation of the stellar population has revealed a metallicity gradient, with an $\sim$0.8 Gyr solar metallicity population in the centre and an $\sim$2-Gyr-old stellar population in the outer parts with sub-solar metallicity of $[M/H] \sim -0.5$ (Mitzkus et al. 2017).

3 EXTRACTING THE SBF SPECTRUM

In this section, we first describe the standard SBF method that is used for analysing imaging data. We then describe the modifications that are necessary to apply the method to IFS data.

3.1 Measuring SBF from images

The standard approach of measuring SBF from images (Tonry & Schneider 1988) starts with constructing a spatial mask of all extended and point sources as well as bad pixels. It is assumed that the sky flux has been accurately subtracted from the image during the data reduction. A smooth surface brightness (SB) model m is constructed for the galaxy. By subtracting the model from the data d, the brightness fluctuations become visible but are still proportional to the square root of the SB model. We call this the preliminary residual image

$$r' = d - m. \tag{1}$$

The spatial mask is complemented by masking all unwanted objects that show up on the preliminary residual image, such as foreground stars, globular clusters (GCs), and image defects. To remove remaining large-scale structures, the preliminary residual image is smoothed on a scale of $\sim$10 times the point spread function (PSF) FWHM. We also renormalize the image to bring the fluctuations to a common level (e.g. Tonry & Schneider 1988; Pahre & Mould 1994; Pahre et al. 1999; Dunn & Jerjen 2006)

$$r = \frac{r' - r'_{\mathrm{smooth}}}{\sqrt{m}}. \tag{2}$$

The masked residual image is then Fourier-transformed and the power spectrum $P(f)$ is computed. The smoothing impacts the power spectrum at the lowest frequencies f (Tonry & Schneider 1988); therefore, these need to be masked in the later analysis.

The data power spectrum is fitted with

$$P(f) = P_0 E(f) + P_1, \tag{3}$$

where P_0 is the SBF flux at $f = 0$ and P_1 measures the photon shot noise, which is presumed to be constant (white noise) in equation (3) but is affected by the pixel interpolation scheme, as described below. The expectation power spectrum $E(f)$ is obtained by convolving the mask power spectrum with the PSF power spectrum (this is mathematically not rigorous but a very practical approximation; see remarks by Jensen, Tonry & Luppino 1998).

By assuming that P_0 is the SBF flux at $f = 0$, we ignore that undetected GCs add some power to P_0. It is possible to correct for this power (e.g. Tonry & Schneider 1988) by estimating the GC

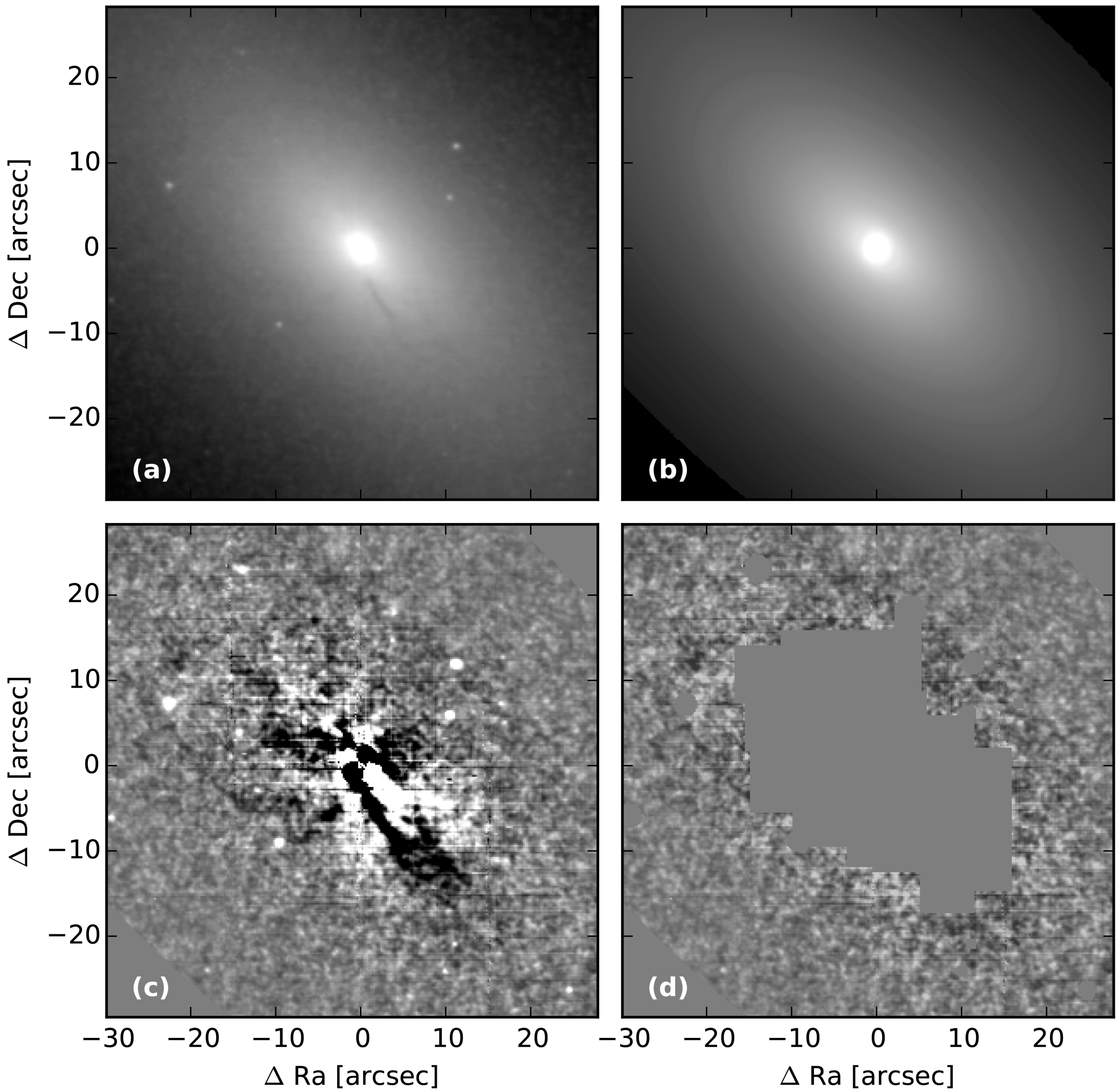

Figure 1. (a) The white-light image of NGC 5102, obtained by collapsing the MUSE data cube along the spectral dimension. Spectral layers that are affected by nebular or sky emission have been masked out. (b) The SB model of NGC 5102. (c) Preliminary residual image, the difference between the white light and the model images. The most prominent residuals are point-like sources and dust obscuration that also influence the fit in the centre. (d) Fluctuation (residual) image with point sources and dust masked.

luminosity function from the detected GCs. In the case of NGC 5102, this is not necessary, because this low-mass S0 galaxy has only a small number of GCs.

3.2 Adapting the procedure to measure the SBF spectrum

Extracting the SBF spectrum from IFS data cubes, the MUSE data cubes in particular, requires some adjustments to the traditional approach presented in the previous section. This starts with creating a white-light image from the data cube. In principle, one could just collapse the data cube along the dispersion dimension to create the white-light image, but this would neglect the influence of nebular and sky emission lines. Since NGC 5102 has some prominent nebular emission lines that might affect a fit of the stellar SB, we mask (in the spectral dimension) those lines. Conservatively we also mask the brightest 100 sky lines, because at these wavelengths the residuals of the sky subtraction and of the underlying image-slicer system of MUSE are most prominent.[1] The white-light image is obtained by averaging all unmasked wavelength layers of the data cube. We illustrate this step for our data in Fig. 1(a).

We also cut the data cube in all three dimensions (lower and upper wavelength cut and at all four edges in the spatial plane) to remove the regions that had not received fully homogeneous coverage.

[1] A quantitative assessment of the importance of the image-slicer system is difficult. In order to measure the power spectrum imprinted by the image-slicer pattern, one would need a perfectly homogeneous illuminated field, which is not achieved in practice. As deviations from homogeneity would leave their own signal in the power spectrum, we decided to mask those wavelength regions that are most affected by the image-slicer residuals.

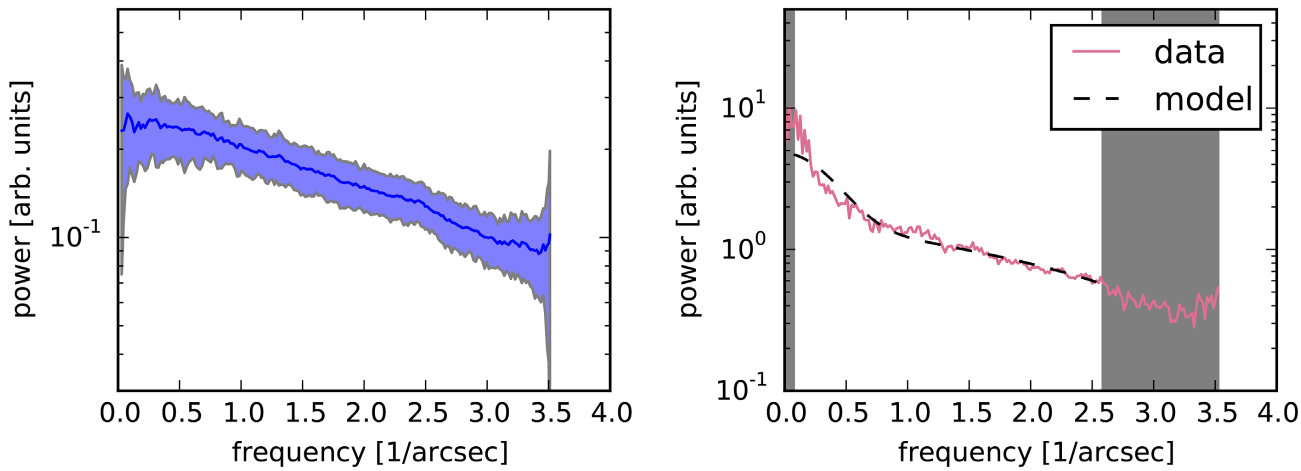

Figure 2. Left: Effect of the drizzling on the power spectrum of initially white noise. The plotted power spectrum is the average power spectrum of 81 spectral layers of a mock data cube that was drizzled with the MUSE data reduction software from a pixtable filled with white-noise mock data. The shaded area is the 1σ standard deviation on the 81 power spectra. Right: The data power spectrum at 6500 Å (solid violet line) with the corresponding fit (dashed black line). Shaded regions have been excluded from the fitting. For display reasons, the power spectra have been azimuthally averaged; the analysis is done on the full 2D versions of the power spectra.

We compute the smooth SB profile from the white-light image with the ELLIPSE task in the STSDAS IRAF package. ELLIPSE fits a number of elliptical isophotes to the input image, without further parametrizing the global shape of the SB. We use the BMODEL task to create the SB model from the set of ellipses fitted with ELLIPSE. The SB model is shown in Fig. 1(b).

The preliminary residual image, the difference between the white-light and the model image, is shown in Fig. 1(c). On this image, there are a number of point-like objects that we mask by visual inspection of the image. More importantly, in the centre of the galaxy there are strong residuals. This is probably due to dust absorption that also affects the SB fit in the centre. We mask those regions completely and are left with the pure fluctuation image shown in Fig. 1(d).

The next step is the renormalization of every monochromatic layer of the data cube (see equations 1 and 2). For this we scale the SB model to the monochromatic layer under consideration. The scaling constant is the ratio of the mean object flux in that monochromatic layer and the mean flux of the SB model. We subtract the scaled SB model from the data to obtain the preliminary residual image (equation 1). This image is smoothed with a 2D Gaussian with a FWHM of 40 pixels, about 10 times the PSF FWHM. We remove remaining large-scale galaxy features by subtracting the smoothed version from the preliminary residual image. Finally, we divide by the square root of the scaled SB model to obtain the renormalized residual image (equation 2).

The data power spectrum is computed by multiplying the renormalized residual image with a window function and Fourier transforming the product. The window function we use is the product of the spatial mask [the mask that is applied to Fig. 1(d)] and a Hanning function. The Hanning window function suppresses the alias signal in the power spectrum caused by the edges of the detector. The 1D Hanning function is defined as

$$H(n) = 0.5 - 0.5\cos\left(\frac{2\pi n}{M-1}\right) \qquad 0 \le n \le M-1 \tag{4}$$

where M is the number of data pixel, i.e. the length of the Hanning function. The 2D version is obtained via the outer product of two Hanning functions. The power spectrum is the square of the absolute value of the Fourier transform.

As mentioned in Section 2.1, the MUSE data reduction software uses a drizzling algorithm to resample the data from the CCD space to the final data cube. To test the influence of this drizzling on the noise properties, we used pixtables filled with original white noise and the MUSE data reduction software to compute the final mock data cube. An example of such a power spectrum is shown in the left panel of Fig. 2. From this plot, we see that the originally white noise (with a constant power spectrum) becomes a power spectrum that linearly decreases with the frequency f. This means that the drizzling of the MUSE data introduces non-negligible correlations of the white noise and we have to modify equation (3) to fit the data power spectrum. We find that

$$P(f) = P_0 E(f) + P_1 + P_2 f \tag{5}$$

reproduces the observed power spectrum well. We fit for the three constants P_0, P_1, and P_2 in every monochromatic layer, using a non-linear least-squares fitting algorithm. Before fitting the power spectrum, we apply a frequency mask: We cut the smallest frequencies $f < 0.07\,\mathrm{arcsec}^{-1}$, because these are affected by the smoothing of the residuals, and the highest frequencies $f > 2.6\,\mathrm{arcsec}^{-1}$, because these contain only information about the noise properties and would bias the fit in an unwanted way. In the right panel of Fig. 2 we show an example fit of the power spectrum where the power spectra have been azimuthally averaged for clarity.

In order to compute the expectation power spectrum, we first compute the PSF and window-function power spectra. The PSF power spectrum is computed by multiplying the PSF image with the Hanning function prior to the Fourier transformation. The window-function power spectrum is obtained by Fourier transforming the product of the spatial mask and the Hanning function. The expectation power spectrum $E(f)$ is the convolution of the PSF and the window-function power spectrum.

As mentioned at the beginning of the section, we apply the described steps to every monochromatic layer of a MUSE data cube. This gives about 3600 SBF measurements at different wavelengths – an SBF spectrum.

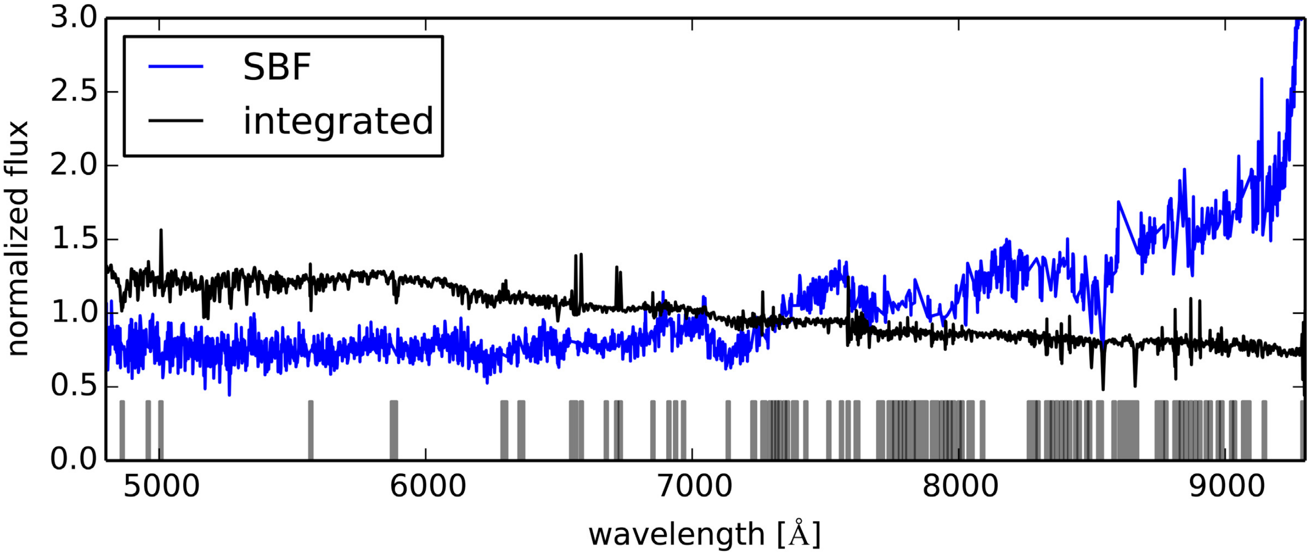

Figure 3. The integrated spectrum (black) and the SBF spectrum (blue) of NGC 5102 obtained from the MUSE observations. The regions marked in grey have been masked in the SBF spectrum, as these wavelengths are contaminated either by gas emission in NGC 5102 or by atmospheric emission lines. No masking has been applied to the integrated spectrum, because sky line residuals should average out during summation and gas emission lines are visible.

We estimate the SNR of the SBF spectrum at each spectral pixel from the ratio (Pahre et al. 1999; Jensen et al. 2001)

$$\mathrm{SNR}(\lambda) = \frac{P_0(\lambda)}{P_1(\lambda)}. \tag{6}$$

The integrated spectrum and the SBF spectrum of NGC 5102 are shown in Fig. 3. The integrated spectrum is the sum of all spectra at unmasked positions in Fig. 1(d). We masked a number of wavelengths in the SBF spectrum (grey shaded regions in Fig. 3) due to the following two reasons: The gas emission in the galaxy outshines the stellar SBF (e.g. H α, H β, [O I] $\lambda\lambda$ 6300, 6364, [O III] $\lambda\lambda$ 4959,5007, [N II] $\lambda\lambda$ 6548, 6583, [S II] λ 6716 and [S II] λ 6731) and the second major contamination is due to sky lines. At the positions of sky lines, the residual data cube is dominated by the pattern of the image-slicer system MUSE is using. The overall shape of the SBF spectrum is very different from that of the integrated spectrum: While the integrated spectrum decreases with increasing wavelength, the SBF spectrum increases with increasing wavelength. The blue part of the SBF spectrum is flat. The strongest features that we see are molecular bands in the wavelength region between 6000 and 8000 Å.

4 COMPARISON OF THE SBF SPECTRUM WITH STELLAR SPECTRA

SBFs are dominated by the most luminous stars in a population. In intermediate-age and old stellar populations, these are RGB and (TP-)AGB stars. To a first degree approximation, TP-AGB spectra come in two flavours: stars that are oxygen rich (spectral type M) and stars with carbon-rich atmospheres (spectral type C). Main-sequence stars have typically oxygen-rich atmospheres with C/O < 1.0. During the third dredge-up C/O increases, transforming initial M-type stars into C-type stars. The change from an oxygen- to a carbon-rich atmosphere does not only become apparent through spectral features but is also of relevance for the opacity and other fundamental parameters (e.g. Marigo et al. 2013). The frequency of M- and C-type stars is metallicity dependent (Battinelli & Demers 2005; Cioni 2009) and a dependency on age is debated (Feast, Abedigamba & Whitelock 2010; Kacharov, Rejkuba & Cioni 2012).

Extrapolating the C/M star ratio metallicity relation by Battinelli & Demers (2005) and Cioni (2009) to a metallicity of [Fe/H] = -0.5, broadly the value representative for NGC 5102, consistently predicts the fraction of C-type stars to be at most 4 per cent by number. Given that RGB and AGB stars will contribute to the SBF spectrum, we do not expect to see a strong signal from carbon stars in the NGC 5102 spectrum. The relative brightness of M- and C-type AGB stars depends on several parameters, most notably on age and metallicity. Generally it is found that massive bright M-type AGB stars are predominantly seen in metal-rich populations. Cioni & Habing (2003) show that in the Large Magellanic Cloud M-type AGB stars can be as bright as the C-type stars. Given the relative high metallicity of NGC 5102, we conclude that 4 per cent C-type stars by number will not make a significant contribution to the luminosity of the stellar population.

To test this expectation, we compare the NGC 5102 SBF spectrum to stellar spectra. We use the data release 1 (DR1) spectra from the X-shooter spectral library (XSL; Chen et al. 2014), because this library provides M- and C-type spectra. Most of these spectra cover the wavelength range from 3000 to 10 200 Å, much larger than the MUSE wavelength range. The wavelength coverage is an important advantage of XSL over other libraries, because it allows us to compare the spectra over the full MUSE wavelength range. The XSL resolution of 10 000 is much higher than what we need, and therefore we broaden the XSL spectra with a Gaussian line-spread function of 2.5 Å to bring them to the MUSE resolution.

From the XSL DR1 database G27,[2] we obtained the spectra of 'M-type' and 'carbon-related' stars. For most of the M-type stars, we obtained the metallicity, effective temperature, and surface gravity values from Chen (2013).

To compare the SBF spectrum with XSL spectra, we mask sky and emission lines (as in Fig. 3) and missing parts of the XSL spectra (i.e. close to 6400 Å or in other regions with missing data).

[2]Available from http://xsl.u-strasbg.fr/

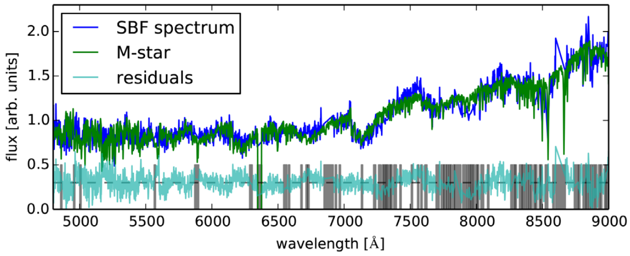

Figure 4. The SBF spectrum of NGC 5102 is shown in blue. The best-fitting M-type stellar spectrum from the XSL DR1 library is shown in green. The residuals (SBF − M-type spectrum) are shown in turquoise. Most of the dominant spectral features, including the molecular bands, are well represented by the M-type stellar spectrum, meaning that M-type giants and supergiants are the dominant type of stars contributing to the SBF signal of this galaxy. Grey regions are masked for the $\chi^2_{\rm red}$ computation, either because sky lines and emission lines do not permit us to measure the SBF or because the XSL spectrum is missing.

To avoid numerical issues, we normalize the SBF and the stellar spectra by their mean values. We compute a reduced χ^2 via

$$\chi^2_{\rm red} = \frac{1}{\rm DOF} \sum_i \frac{\left[F^{\rm SBF}_{\rm data}(\lambda_i) - P(n, x_i, \boldsymbol{a}) F_{\rm XSL}(\lambda_i)\right]^2}{\varepsilon^2(\lambda_i)}. \quad (7)$$

Where the degrees of freedom (DOF) are the number of unmasked spectral pixels, x_i maps the wavelength array into the interval [− 1, 1] and $P(n, x, \boldsymbol{a})$ is the sum of the first $n + 1$ Legendre polynomials $P_i(x)$

$$P(n, x, \boldsymbol{a}) = \sum_{i=0}^{n} a_i P_i(x), \qquad x \in [-1, 1]. \quad (8)$$

The coefficients a_i of the multiplicative Legendre polynomial are determined such that the $\chi^2_{\rm red}$ is minimized. We find that $n = 11$ is needed to correct continuum differences between the observational SBF spectrum and the XSL stellar spectra. The error ϵ in equation (7) is a smoothed version of the $P_1(\lambda)$ spectrum (see equation 6), using a 100 pixel running mean for smoothing.

We find, as expected, that the M-type spectra reproduce the SBF spectrum very well. The best-fitting M-type star is SMC046662. The spectrum of this star and the SBF spectrum are shown in Fig. 4. All dominant molecular features are very well traced by the M-type stellar spectrum. In Appendix A we investigate the sensitivity of the SBF spectrum to detect a marginal fraction of carbon stars. We emphasize that below 5500 Å the flux of the XSL spectrum is strongly increased by the multiplicative polynomial. Most likely below 5500 Å hotter stars start to dominate the SBF spectrum. In this region, the match between the SBF spectrum and the M-type stellar spectrum gets worse.

Given that an M-type spectrum is quite a good representation of the SBF spectrum, we compute the $\chi^2_{\rm red}$ for all M-type stars for which we have metallicity, effective temperature, and surface gravity values. In Fig. 5 we plot $\chi^2_{\rm red}$ as a function of effective temperature and surface gravity. We see that the best-fitting M-type spectra are those of warm M-type stars. The temperatures of the best-fitting stars are in the range 3000 to 4000 K. The surface gravity is much less constrained, which is not entirely surprising as only high-resolution spectroscopy is capable of providing accurate information on log g. There are two outlier points in Fig. 5. The spectrum at 4200 K does not give a good fit; it is missing the characteristic molecular features. The spectrum at log g = 3.5 provides an acceptable fit. This point is substantially offset in log g. It is,

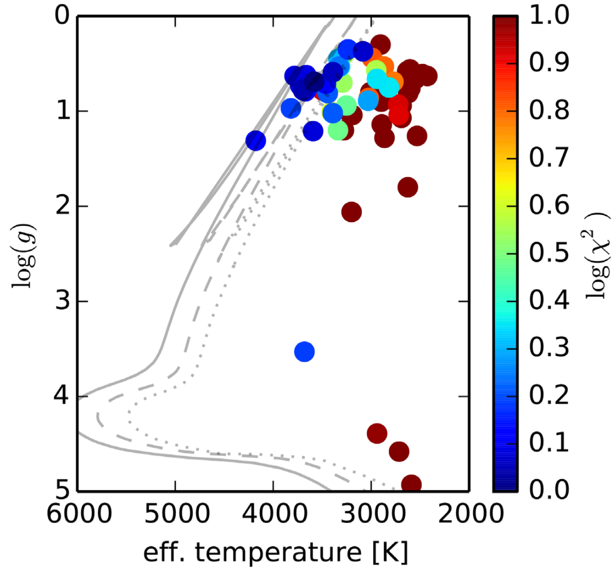

Figure 5. For all M-type stars in the XSL library (with temperature and surface gravity values in Chen 2013), their ability to describe the NGC 5102 SBF spectrum is shown in terms of $\chi^2_{\rm red}$. To guide the eye, we plot in grey the 10-Gyr-old PARSEC isochrones with [Fe/H] of −0.5 (solid line), 0.0 (dashed line), and +0.5 (dotted line). This plot reveals that warm M-type stars are the best-fitting type of stars to the SBF spectrum of NGC 5102. log($\chi^2_{\rm red}$) values have been clipped at 1.

however, beyond the scope of this paper to evaluate whether the log g values that we have adopted from Chen (2013) are robust. The constraints on metallicity are even poorer; spectra with $-1.5 \lesssim$ [Fe/H] $\lesssim 0.0$ provide acceptable fits.

5 MODELLING THE SBF SPECTRUM

Many stellar population synthesis models have been made public (e.g. Bruzual & Charlot 2003; Maraston 2005; Raimondo et al. 2005; Coelho et al. 2007; Mollá, García-Vargas & Bressan 2009; Vazdekis et al. 2010, 2012). Other authors additionally provide their codes (e.g. Leitherer et al. 1999; Le Borgne et al. 2004; Conroy et al. 2009). None of these provide model SBF spectrum predictions. Therefore, we had to compute our own model predictions. We name our models 'Stellar Population for All Applications' (SPAA).

5.1 Stellar evolution models

We use PARSEC isochrones as input to our stellar population synthesis code. The PARSEC stellar evolution code (Bressan et al. 2012) is a revised version of the former Padova stellar evolution codes. Bressan et al. (2012) update the stellar input physics by using the solar composition from Grevesse & Sauval (1998) with some elemental abundances taken from Caffau et al. (2011). The stellar evolution models are computed for stars in the mass range $0.1 \le M/{\rm M}_\odot \le 12$ and with chemical compositions in the range $0.0005 \le Z \le 0.06$. The helium abundance of a solar-scaled model is computed from the metal abundance Z following $Y = 0.2845 + 1.78Z$. PARSEC traces the stellar evolution from the pre-main-sequence up to the onset of the TP-AGB evolution with the first thermal pulse.

The evolution of TP-AGB stars is traced with the dedicated COLIBRI code (Marigo et al. 2013). The COLIBRI calculations are initialized with the parameters of the PARSEC stellar model at the first thermal pulse. There are two different approaches to modelling TP-AGB evolution: 'full models' that solve the time-dependent equations of stellar structure and 'synthetic models' that use analytic relations (calibrated against full model predictions) to describe the evolution between two thermal pulses. For a discussion of the strengths and weaknesses of both approaches, we refer the reader to Marigo et al. (2013). The COLIBRI code is based on a hybrid approach, calculating the equation of state, opacities, and nuclear reaction rates on the fly and using fitting functions, e.g. the efficiency of the third dredge-up (for details see Marigo et al. 2013). We use the COLIBRI PR 16 extension to include the AGB stars in the isochrone predictions (Rosenfield et al. 2016; Marigo et al. 2017).

At the time of writing this paper, PARSEC isochrones had been published only for solar-scaled abundances. Therefore, all SPAA SSP spectra have been computed with solar-scaled abundances. Especially elliptical galaxies often show α-element enhanced abundances (e.g. Worthey, Faber & Gonzalez 1992; Trager et al. 2000a,b; Zhu, Blanton & Moustakas 2010; Greene et al. 2013), so the restriction to solar-scaled abundances might bias the results. Recently Fu et al. (2018) reported on the first PARSEC stellar evolution models that deal with α-element enhanced abundances. These models will be publicly available in the future.

5.2 Stellar spectral libraries

We decided to make use of two stellar spectral libraries: the theoretical library of Coelho (2014) and the observational MILES library (Sánchez-Blázquez et al. 2006).

The theoretical stellar spectral library by Coelho (2014) has been computed with the specific aim of being used for stellar population synthesis models. The library consists of opacity distribution functions, model atmospheres, statistical samples of surface fluxes [spectral energy density (SED) models] and high-resolution stellar spectra (Coelho 2014). Only the high-resolution spectra are needed in this work for the purpose of computing SSP spectra.

We briefly summarize the most important features of the computation and refer the reader to Coelho (2014) for the details. The model atmospheres were computed with the LINUX port of the ATLAS9 code (Kurucz 1970; Sbordone et al. 2004), which assumes plane-parallel geometry and local thermodynamic equilibrium. For stars cooler than 4000 K, pre-computed MARCS (Gustafsson et al. 2008) model atmospheres were used as these compute spherically symmetric model atmospheres (especially important for giant stars) with a larger set of molecular opacities (important for cool stars in general). High-resolution spectra are computed with the LINUX port of the SYNTHE code (Kurucz & Avrett 1981; Sbordone et al. 2004) for the wavelength range $2500 \leq \lambda \leq 9000$ Å.

An important feature of the models is that they are corrected for the effect of weak absorption lines that mainly affect the pseudo-continuum shape in the blue part of the spectrum. Coelho (2014) uses low-resolution SEDs to correct the continuum of the high-resolution spectra in a differential approach (see her fig. 3).

The coverage of the $\log(g)$–$T_{\rm eff}$ plane of this stellar spectral library is not regular as it follows the locus of the isochrones (Coelho 2014). The range of temperature covered is $3000 \leq T_{\rm eff} \leq 25\,000$ K, the range of surface gravity is $-0.5 \leq \log(g) \leq 5.5$, and four solar-scaled chemical compositions are provided for [Fe/H] = [−1, −0.5, 0.0, 0.2]. All SSP models that are based on the Coelho (2014) theoretical stellar spectra are labelled 'SPAA/Coelho' in this paper. The same stellar spectra are also used in a forthcoming paper by Coelho, Bruzual & Charlot (Coelho et al., private communication) to update the Coelho et al. (2007) SSP spectra.

We also use the observational MILES stellar spectral library (Sánchez-Blázquez et al. 2006) as input for our SSP model spectra. The MILES stellar spectral library consists of 985 stars, where the selection of stars is optimized for stellar population synthesis. The stars were observed with the 2.5 m Isaac Newton Telescope and the wavelength range covers $3525 \leq \lambda \leq 7500$ Å. Special attention has been paid to avoid flux losses due to differential atmospheric refraction and to guarantee a good flux calibration (Sánchez-Blázquez et al. 2006). The spectral resolution of the MILES stellar spectral library has been independently assessed by several authors, consistently finding a FWHM resolution of 2.55 Å (Beifiori et al. 2011; Falcón-Barroso et al. 2011; Prugniel, Vauglin & Koleva 2011).

In addition to the MILES spectra, we use the stellar parameters derived by Cenarro et al. (2007) following the procedure described in Cenarro et al. (2001). In summary, for field stars the parameters are based on an extensive literature search and an iterative procedure to homogenize these published parameters. For cluster stars, the metallicity, temperature, and surface gravity are obtained from scaling relations: The metallicity is tied to the metallicity scale of Carretta & Gratton (1997), temperatures are derived from colour–temperature relations (Alonso, Arribas & Martinez-Roger 1996; Alonso, Arribas & Martínez-Roger 1999), and surface gravities are derived by matching the stars to isochrones (from Girardi et al. 2000) in the M_V–$T_{\rm eff}$ plane.

We found that the spectra in the MILES library are not scaled to common flux units. We follow the flux calibration that Prugniel & Soubiran (2001) used for the ELODIE library: They have scaled the flux of the stars to 1 at 5500 Å. We did the same for all MILES stars, then multiplied with the flux of a theoretical PHOENIX spectrum (Husser et al. 2013) of similar surface gravity, effective temperature, and chemical composition at the same wavelength. All SSP models that are based on the empirical MILES stellar spectra are labelled 'SPAA/MILES' in this paper.

5.3 Synthesis of single-burst stellar populations

We implemented the widely used isochrone synthesis approach (e.g. Charlot & Bruzual 1991; Bruzual & Charlot 2003; Coelho et al. 2007; Conroy et al. 2009; Vazdekis et al. 2010, 2012) to compute the SSP model spectra. The isochrone synthesis approach consists of a summation over all points i of an isochrone of given age t and chemical composition, parametrized by the iron abundance [Fe/H]

$$F_{\rm SSP}(t, [{\rm Fe/H}]) = \sum_i \rho_i(m_i) F([{\rm Fe/H}], T_{{\rm eff},i}, \log\, g_i). \tag{9}$$

$F([{\rm Fe/H}], T_{{\rm eff},i}, \log\, g_i)$ is the spectrum of a star with the specified parameters and $\rho_i(m_i)$ is the initial mass function (IMF) weight, integrated over a small mass interval around m_i:

$$\rho_i(m_i) = \int_{m_i-\Delta m_i}^{m_i+\Delta m_{i+1}} \xi(\log m) {\rm d}\log m, \tag{10}$$

$$\Delta m_i = \left|\frac{m_i - m_{i-1}}{2}\right|. \tag{11}$$

We use a Chabrier (2003) IMF

$$\xi(\log m) = \begin{cases} 0.158 \exp\left[-\frac{(\log m - \log 0.079)^2}{2\times 0.69^2}\right] & \text{if } \log m \leq 0 \\ 0.0443 m^{-1.3} & \text{if } \log m > 0 \end{cases} \tag{12}$$

5.4 Validation of our SSP library

To validate that the SPAA code is numerically correct and the results are compatible with other published SSP spectrum models,

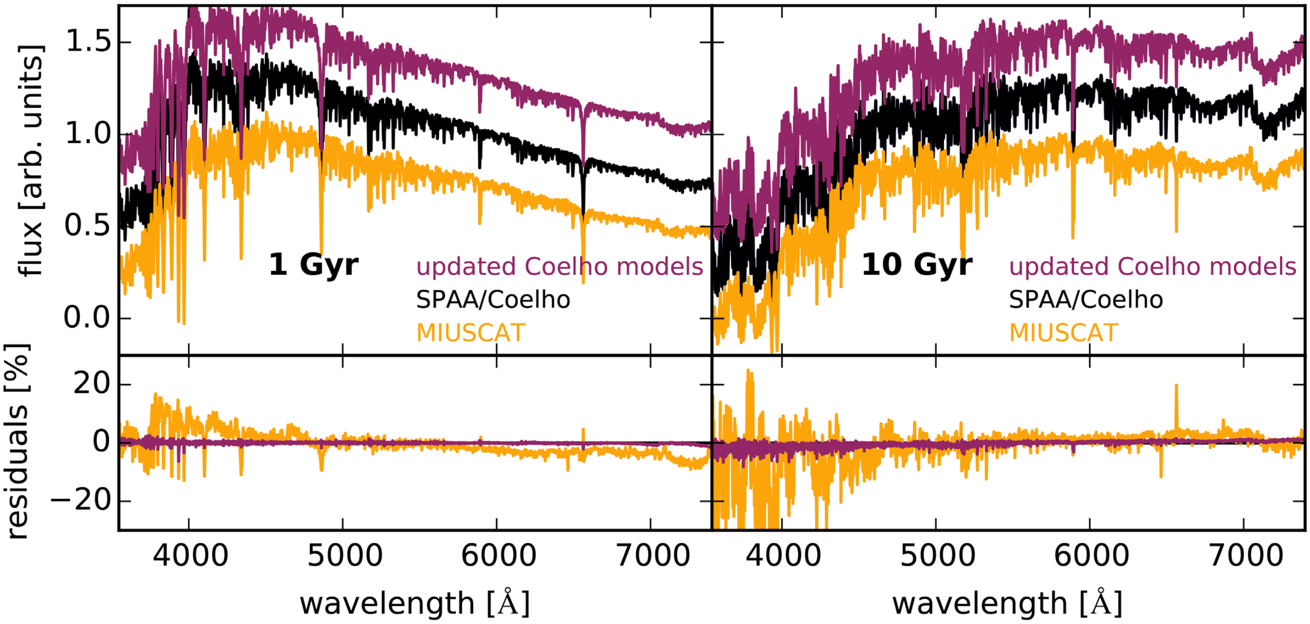

Figure 6. Comparison of our SPAA/Coelho SSP model spectra (black) to the corresponding ones from the updated version of the Coelho SSP library (violet) and the MIUSCAT SSP library (orange) for two ages. The spectra are convolved to a common resolution of 2.5 Å FWHM and interpolated to a common wavelength grid. The spectra have been normalized with the scalar mean value and for better visibility the Coelho and MIUSCAT spectra are offset by ±0.3, respectively. The bottom panel shows the difference spectrum divided by the SPAA/Coelho spectrum; colours are the same as in the upper panels.

we used two other stellar population synthesis models as comparison: the MIUSCAT (Vazdekis et al. 2012) SSP library and the yet unpublished SSP models from the updated version of the Coelho models. This choice is motivated by the fact that these two SSP libraries make use of the two stellar spectral libraries that we use in SPAA.

The updated version of the Coelho SSP models use PARSEC isochrones, Chabrier (2003) IMF, and Coelho (2014) stellar spectra. These spectra are therefore based on the same inputs as the SPAA/Coelho models. The MIUSCAT SSP library is based on BaSTI isochrones (Pietrinferni et al. 2004) and a Kroupa (2001) universal IMF. We had to make the compromise of using a different IMF and isochrone for the comparison with the SPAA/MILES models because the MIUSCAT models do not use the PARSEC isochrones and Chabrier (2003) IMF. For the IMF, however, the Kroupa (2001) universal IMF and the Chabrier (2003) one are reasonably similar, so we do not expect these small differences to influence the evaluation of the SSP spectra.

In Fig. 6, we compare a 1 Gyr and a 10 Gyr solar metallicity population from our SPAA/Coelho models to the corresponding MIUSCAT and updated version of the Coelho SSP models. This plot shows that the residuals between the SPAA/Coelho and the updated version of the Coelho SSP models are flat. We therefore conclude that SPAA works well numerically.

The increased scatter in comparison with the MIUSCAT models is caused by differences in the input stellar spectra. For the 1 Gyr model the residuals between SPAA/Coelho and MIUSCAT are reminiscent of an A-type star spectrum. These residuals are caused by the different isochrones used: The PARSEC isochrone is slightly hotter at the main-sequence turn-off for young ages (see also Gallart, Zoccali & Aparicio 2005). We have verified that the residuals are flat when we compute SPAA models with BaSTI isochrones. The differences between the two isochrones are much smaller for older ages, as is also seen by less systematic difference in the right panel of Fig. 6.

5.5 Synthesis of SBF model spectra

The definition of SBF is given in equation 9 of Tonry & Schneider (1988):

$$\bar{L} = \frac{\sum_i n_i L_i^2}{\sum_i n_i L_i} \tag{13}$$

where i are the different types of stars, L_i is the luminosity, and n_i is the number of stars of type i. The transition to spectra is simple, by just replacing the luminosity with the spectrum and n can be identified as the IMF weight $\rho_i(m_i)$. Therefore, computing theoretical SBF spectra of SSPs is straightforward.

The SBF spectra of complex stellar populations are, however, no longer linear combinations of the SSP SBF spectra (Liu et al. 2002). In order to keep the idea and flexibility of SSPs also in the context of SBF spectra, we compute the numerator and denominator of equation (13). The denominator is just the integrated spectrum that we already described in equation (9). The numerator is then

$$F_{\mathrm{SSP}}^{\mathrm{var}}(t, [\mathrm{Fe/H}]) = \sum_i \rho_i(m_i) \left\{ F([\mathrm{Fe/H}], T_{\mathrm{eff},i}, \log\, g_i) \right\}^2 . \tag{14}$$

We call this the variance spectrum. The ratio of the variance spectrum and the integrated spectrum is the SSP SBF spectrum.

Any SBF spectrum with a complex SFH $\omega(t, [\mathrm{Fe/H}])$ is then computed from the pre-computed libraries via

$$F_{\mathrm{SBF}} = \frac{\sum_t \sum_{[\mathrm{Fe/H}]} \omega(t, [\mathrm{Fe/H}]) F_{\mathrm{SSP}}^{\mathrm{var}}(t, [\mathrm{Fe/H}])}{\sum_t \sum_{[\mathrm{Fe/H}]} \omega(t, [\mathrm{Fe/H}]) F_{\mathrm{SSP}}(t, [\mathrm{Fe/H}])} . \tag{15}$$

5.6 Testing the influence of different ingredients on the SBF spectrum

In this section, we compare the SBF spectra with the integrated spectra and highlight the differences between both diagnostics. The other focus is the comparison of the two different SSP libraries we computed, SPAA/MILES and SPAA/Coelho.

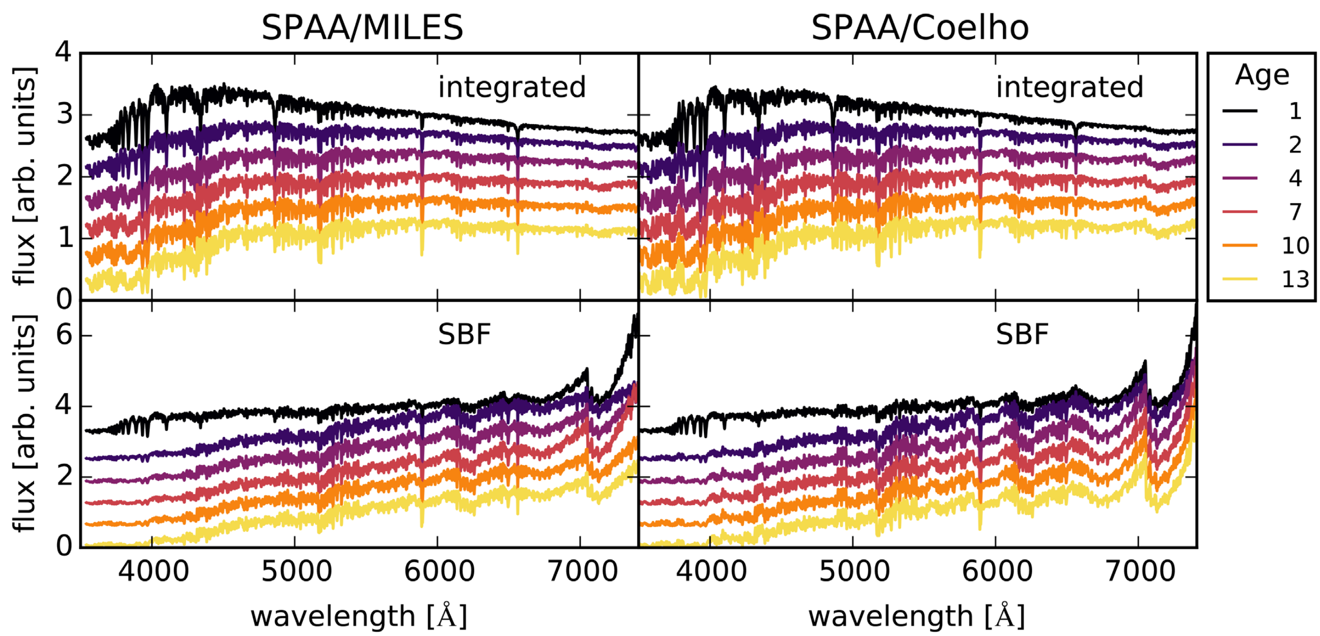

Figure 7. The age evolution of the model SSP spectra of a solar metallicity population. The left-hand panel shows the SPAA/MILES models, the right-hand panel the SPAA/Coelho ones. The top row plots the age evolution of the integrated spectrum, the bottom row the evolution of the SBF spectrum. We find that the SPAA/Coelho library predicts stronger molecular bands than the SPAA/MILES models. The ages are given in Gyr.

In Fig. 7 we show the age evolution of the spectrum of a solar metallicity population. By comparing the SBF and the integrated spectra of the same age, we see that the SBF spectrum is dominated by much cooler stars than the integrated spectrum. There are two indicators for that: The pseudo-continuum of the SBF spectrum keeps rising with increasing wavelength, while for the integrated spectra the maximum flux is within the plotted wavelength range. Also the appearance of the molecular features around 7000 Å is an indicator that the stars dominating the SBF spectrum are cooler. This suggests that the SBF spectrum is dominated by the cooler giant stars.

The metallicity variance of a 5-Gyr-old stellar population is shown in Fig. 8. We see that the molecular features become relevant at the transition from [Fe/H] = −1.0 to −0.5. While the metal-poor population shows many metal absorption lines, there are no molecular features seen. This is caused by the fact that with increasing metallicity, the giant branch temperature becomes cooler and at some point molecules can form.

In order to quantify the differences between the two models, we compare the root mean square (RMS) of the difference spectrum in four different wavelength sections of ∼1000 Å length. In Fig. 9 we plot the difference for the wavelength range $5500 \leq \lambda \leq 6500$ Å for the integrated and the SBF spectra. From the comparison of the integrated spectra, we see that the RMS increases with increasing age. This is a systematic trend that we observe independently from wavelength. These systematic differences are mainly driven by differences in the line strengths. For the 1 Gyr spectrum, the most important mismatch is the Mg*b* feature; for older populations a blend of a Ca I and an Fe I line at ∼6463 Å is the most important difference. The high RMS values for the [Fe/H] = −1.0 spectra are caused by continuum mismatches that dominate the RMS. The best agreement between the two libraries is seen for spectra with [Fe/H] = −0.5.

In the comparison shown in the right panel of Fig. 9, we see similar trends, however at slightly higher RMS values. The differences between the SBF spectra (right panel of Fig. 9) are mainly caused by stronger molecular features in the SPAA/Coelho SSP models. The situation is slightly different in the [Fe/H] = −1 models. Fig. 8 already reveals that the [Fe/H] = −1 SBF spectra do not show strong molecular features. Therefore, the RMS between the SPAA/MILES and the SPAA/Coelho models at these low metallicities is caused by differences in the atomic line strengths and is therefore much lower than the RMS values for the higher metallicity spectra. For the 1 Gyr population, the SPAA/Coelho predicts molecular features that are not seen in the SPAA/MILES models. For the older populations, differences in the continuum drive the residuals.

We conclude that the integrated spectra agree reasonably well, particularly for higher metallicities. The SBF spectra exhibit more pronounced differences. As these are the first SBF spectra in the literature, we cannot judge which prediction provides the best match.

6 STAR FORMATION HISTORY DETERMINATION

In this section, we describe the derivation of the SFH for NGC 5102 and how we make use of the additional information provided by the SBF spectrum. We start in Section 6.1 with fitting the spatially *integrated* spectrum. As explained in Section 5.5, multicomponent population SBF spectra are not a linear combination of SSP SBF spectra. We therefore explain in Section 6.2 the use of the *SBF* spectrum to further constrain the SFH.

6.1 The integrated spectrum

We measure the SFH from a spatially integrated spectrum of NGC 5102. In order to allow a consistent comparison with the SBF spectrum, we use the same spatial region that is used in the SBF analysis to compute the integrated spectrum. Therefore, we add the spectra at the unmasked spatial positions [see Fig. 1(d)].

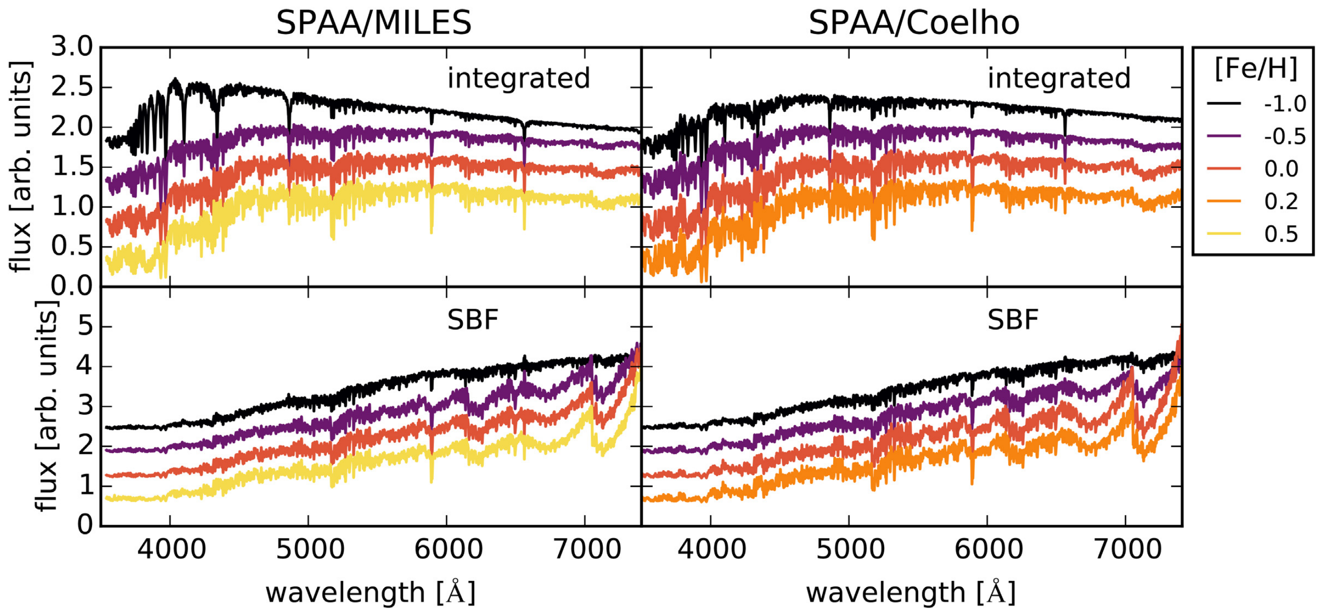

Figure 8. Metallicity variance of a 5-Gyr-old stellar population. Panel positions are as in Fig. 7. SPAA/MILES models cover the metallicity range $-1.0 \leq$ [Fe/H] $\leq +0.5$ in steps of 0.5 dex. SPAA/Coelho models have [Fe/H] = [−1.0, −0.5, +0.0, +0.2].

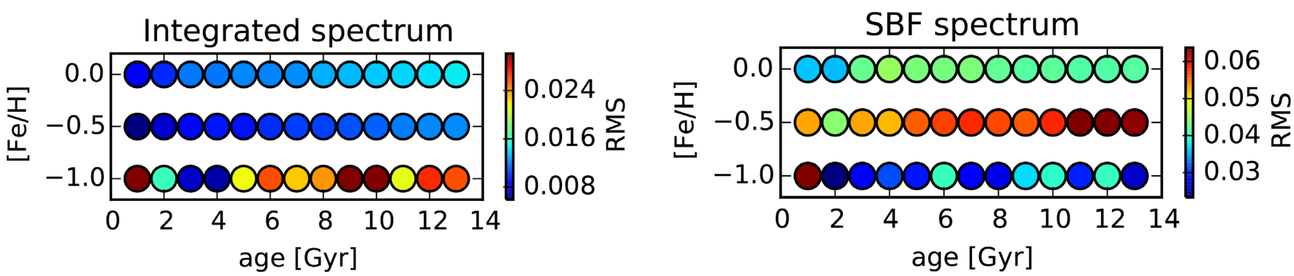

Figure 9. Comparison of the SPAA/MILES and the SPAA/Coelho spectral libraries. The colour of the points gives the RMS of the difference spectrum of the two model spectra in the wavelength range $5500 \leq \lambda \leq 6500$ Å. In the left plot, we compare the integrated spectra, in the right plot the SBF spectra. The colour scale is truncated at the 95th percentile.

We determine the SFH using the full spectrum fitting code PYPARADISE (Husemann et al. 2016), an extended PYTHON version of the PARADISE code (Walcher et al. 2015). PYPARADISE determines a non-parametric SFH by reproducing the integrated spectrum as a weighted linear combination of template spectra. In this work, we use the SPAA SSP spectra as templates: The ages of the template spectra cover the range from 1 to 13 Gyr, sampled in 1 Gyr steps. The metallicities cover [Fe/H] = [−1, −0.5, 0.0, +0.5] for the SPAA/MILES SSP spectra and [Fe/H] = [−1, −0.5, +0.0, +0.2] for the SPAA/Coelho SSP spectra. In both cases, this means that we input 52 SSP template spectra to PYPARADISE.

The determination of the SFH is a two-step process. In Section 6.1.1, we describe the determination of the fiducial best-fitting kinematic and SFH solution. In Section 6.1.2, we describe the bootstrapping to constrain the degeneracy of the SFH.

6.1.1 The initial fit

PYPARADISE starts with logarithmically rebinning the data and template spectra on the same velocity grid. The data spectrum and every template spectrum are individually normalized by their running-mean pseudo-continuum. The running mean is computed with a width of 100 pixels, masking the strong absorption/emission lines (H α λ 6563 and H β λ 4861, the [S II] emission lines at $\lambda\lambda$ 6716, 6731 and the strong [O I] sky line at λ 5577).

We fit three different wavelength regions of the spectrum: H β [4800, 5500], H α [6100, 6900], and Ca II-triplet [8450, 8800]. The continuum normalization is derived from a slightly broader wavelength range. We use an additional 150 Å interval on both sides to avoid edge effects. For the fitting we mask nebular and strong sky emission lines. PYPARADISE fits the kinematic and the SFH successively and iterates this loop. The line-of-sight velocity distribution (LOSVD) is parametrized by a Gaussian and obtained from a Markov chain Monte Carlo (MCMC) run, while keeping the SFH fixed. With the best-fitting LOSVD, the SFH is redetermined via a non-negative least-squares (NNLS) fit. We iterate this loop three times, because tests indicated that this is sufficient to converge to a stable solution. Finally the fiducial best-fitting kinematic and SFH solution are saved. The uncertainties in the LOSVD are derived from the final MCMC run. Since we corrected the radial velocity in the data cube during the data reduction, the LOSVD is mainly the velocity dispersion. We still allow for small velocity shifts because different libraries have slightly different wavelength solutions.

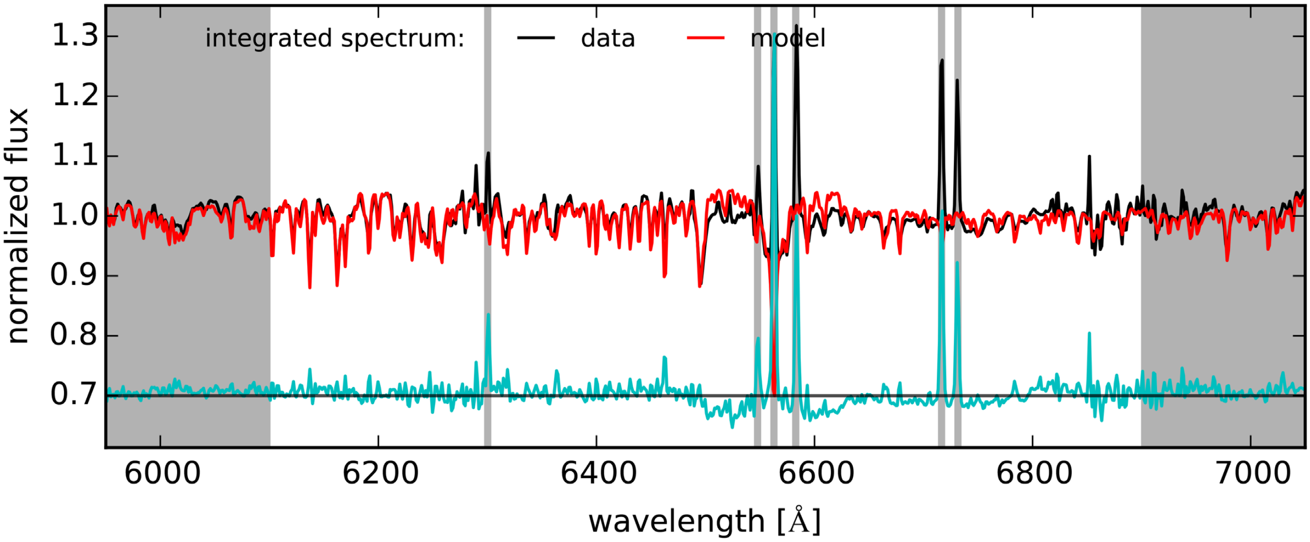

Figure 10. The integrated NGC 5102 MUSE spectrum around the H α feature is shown in black. The best-fitting combination of SPAA/Coelho models is plotted in red. Residuals are plotted in cyan below. The grey areas are masked during the fit; nebular lines are not included in the model fit.

6.1.2 Bootstrapping the SFH

The uncertainties and degeneracies in the SFH are determined via an iterative bootstrapping algorithm (we refer the reader to appendix A of Walcher et al. 2015, for a motivation of the bootstrapping approach). We use 5000 iterations of the bootstrap algorithm. In every bootstrap run the noise of the input spectrum is redistributed with random errors, assuming Gaussian deviations, with the width given by the error spectrum. The LOSVD is randomly chosen from the (Gaussian) distribution determined in the fiducial fit. The number of template spectra is randomly reduced to 80 per cent of the input SSP library. In every bootstrap, the best-fitting SFH is again determined via an NNLS fit, and the corresponding weights are saved. We emphasize that by definition all bootstrapped SFHs have the same χ^2-value, i.e. represent the observed spectrum equally well.

6.1.3 Results from integrated spectrum fitting

We applied the bootstrap strategy to fit the data using our two different sets of SSP-models. For the fit with the SPAA/MILES models, we fit only the two intervals H β and H α in common between data and model. For the SPAA/Coelho models, we fit all three intervals H β, H α, and Ca II-triplet.

Fig. 10 shows the fit of the H α wavelength range with the SPAA/Coelho models. The fitted model is a good representation of the observed spectrum. To ease the evaluation of the 5000 fitted SFHs, we reduce each full SFH to mean luminosity-weighted ages and metallicities. As detailed in Walcher et al. (2015), we derive mean metallicities as average of 'square bracket quantities'. In Fig. 11 every dot represents the average value of one of the 5000 SFHs fitted with the SPAA/Coelho models to the H α wavelength range. In this wavelength interval, we measure an age of 2.2 ± 0.3 Gyr and [Fe/H] $= -0.37 \pm 0.05$. The age of this fit is in good agreement with the values measured by Mitzkus et al. (2017) in the same spatial region, but the metallicities are slightly higher. Mitzkus et al. (2017) use a Voronoi-binned version of the MUSE NGC 5102 data (identical to the data used to derive the kinematics; see Section 2.2) to derive spatially resolved stellar population properties. The data are fitted with the penalized pixel fitting code (PPXF, Cappellari & Emsellem

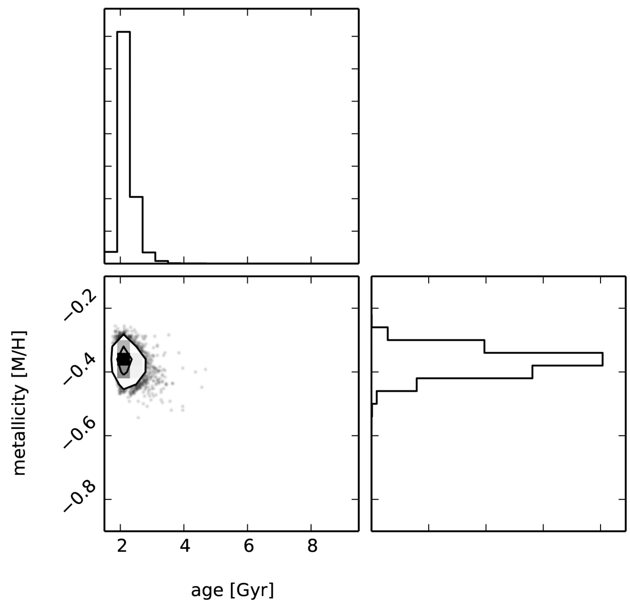

Figure 11. The distribution of luminosity-weighted ages and metallicities, as obtained by fitting the H α region of the integrated spectrum with the SPAA/Coelho models. Every point represents the average luminosity-weighted quantities of a non-parametric SFH fit. In the densest regions, the density of points is represented by grey-scale values. Contour lines are plotted at 0.5, 1.0, 1.5, and 2.0 σ.

2004) using the MIUSCAT SSP spectra (Vazdekis et al. 2012) as templates and fitting the wavelength region from 4750 to 9340 Å simultaneously.

The integrated spectrum fit results to the other wavelength intervals are shown in the appendix. The integrated spectrum with the corresponding SPAA/MILES SSP model is dipplayed in the upper panel in Fig. B1 for H β interval and the corresponding 2D distribution of age and metallicity is shown in Fig. B2. The same plots for the H α interval fitted with SPAA/MILES SSP models are shown in Figs. B3 and B4, the fits with the SPAA/Coelho SSP models are shown in Figs . B5 and B6 for the H β interval and in Figs.

B7 and B8 for the Ca II interval. The discrepancies in the ages and metallicities fitted in different wavelength regions are discussed in Section 7.3.

6.2 Additional constraints from the SBF spectrum

So far we have only used the *integrated* spectrum to derive the SFH, a technique that is well established. In this section, we explain how the SBF spectrum is used to further constrain the SFH. As already mentioned, the SBF spectrum of a complex stellar population cannot be fitted as linear combination of SSP template spectra. It is therefore impossible to fit the SBF spectrum with PYPARADISE in the same way we fitted the integrated spectrum. Instead we use the SBF spectrum to evaluate the SFHs we derived on the integrated spectrum as detailed below.

The bootstrapping provides 5000 different SFHs that all fit the integrated spectrum equally well (in a χ^2 sense). We now test whether all these models represent the SBF spectrum equally well. Therefore, we compute the SBF model spectrum for each of the 5000 SFHs following equation (15) and using the weights assigned to the SSP spectra by PYPARADISE. The next step is to compare the 5000 SBF model spectra with the NGC 5102 SBF spectrum. We do this by computing the reduced $\chi^2_{\rm red}$ via equation (7), where $F_{\rm XSL}$ is replaced by $F^{\rm SBF}_{\rm model}$. We use a third-order multiplicative Legendre polynomial to account for continuum mismatch. In the lower panel of Fig. 12, we compare the NGC 5102 SBF spectrum with the best-fitting SBF spectrum model obtained from the sample of bootstrapped SFHs in the H α wavelength range using the SPAA/Coelho models.

As already discussed in Section 4, the SBF spectrum has higher fluxes than the stellar spectra in the blue part of the spectrum (Fig. 4). The slight upturn below 5200 Å is also not seen in any of the SSP models (see Figs 12, 13, B1, B3, B5, B7). In this region, the SBF model spectrum flux is increased by the multiplicative polynomial to match the data spectrum in Fig. 12. By looking at other SBF model spectrum realizations from the bootstrapping, we found that this upturn can even influence the fit in the red part. We suspect that below ∼5500 Å the SBF spectrum measurement is biased and we are seeing a noise floor. Another common feature is that the SBF model flux around the Mg*b* feature (∼5150 to 5200 Å) is lower than observed. We therefore mask the SBF spectrum below 5500 Å in the subsequent analysis.

We stress that we use different wavelength ranges for the fit of the integrated spectrum and computation of the $\chi^2_{\rm red}$ from the SBF spectrum. The reason for this is that, as argued in the previous paragraph, we find the SBF spectrum below 5500 Å is too noisy. In the red part of the SBF spectrum, the density of the sky lines leads to substantial masking. Combined with the fact that the SPAA/MILES models cut at about 7400 Å we mask the SBF spectrum above 7500 Å entirely for the χ^2 computation. The masked regions are shaded in grey in Fig. 12.

The quality of the SBF spectrum fit depends strongly on the SFH. To emphasize this, we take the SFH from the same bootstrapping of the *integrated* spectrum that leads to the worst-fitting SBF model spectrum and show this in Fig. 13. We recall that by construction both SFHs (i.e. in Figs 12 and 13) fit the integrated spectrum equally well and the plotted integrated spectrum models appear quite similar. However, the differences between the two SBF model spectra in Figs 12 and 13 are easily noticeable. The worst-fitting model has too strong molecular features. The luminosity-weighted ages and metallicities for the best (worst) model are different with an age of 3.0 Gyr (2.6) and a metallicity of [Fe/H] = −0.38 (−0.31). Given these differences between the two model spectra, we expect to be able to better constrain the SFH of NGC 5102 with the additional information from the SBF spectrum.

For the other fit intervals and models, we show the best-fitting SBF spectra with the corresponding integrated spectrum model in the appendix in Figs B1 for H β and B3 for H α with SPAA/MILES models and Figs B5 for Hβ and B7 for Ca II with SPAA/Coelho models.

To quantify the SBF spectrum constraints on the SFH, we use the $\chi^2_{\rm red}$ to compute the probability that the SBF model spectrum represents the data SBF spectrum. We start with scaling the $\chi^2_{\rm red}$:

$$\chi^2_{\rm norm} = {\rm DOF}\frac{\chi^2_{\rm red}}{\min(\chi^2_{\rm red})}. \qquad (16)$$

The $\min(\chi^2_{\rm red})$ is the minimum $\chi^2_{\rm red}$ in one bootstrap sample. The scaling ensures that the best-fitting model has $\chi^2_{\rm norm} = {\rm DOF}$. As van den Bosch & van de Ven (2009) note, in the case of a large number of DOF, the variance in the χ^2 distribution itself becomes non-negligible. The variance of the χ^2 distribution is $\sqrt{2{\rm DOF}}$. For the computation of probabilities based on the $\chi^2_{\rm norm}$, we divide the DOF by the factor $\sqrt{2{\rm DOF}}$. We use the χ^2 statistic to compute the probability p that, even for a correct model, any observation would have a χ^2-value larger than $\chi^2_{\rm norm}$.

$$p(\chi^2_{\rm norm}, {\rm DOF}) = 1 - P\left(\frac{\rm DOF}{2\sqrt{2{\rm DOF}}}, \frac{\chi^2_{\rm norm}}{2\sqrt{2{\rm DOF}}}\right) \qquad (17)$$

$$P(a, x) = \frac{\int_0^x e^{-t} t^{a-1} {\rm d}t}{\int_0^\infty e^{-t} t^{a-1} {\rm d}t} \qquad (a > 0) \qquad (18)$$

In equation (18) we are repeating the definition of the incomplete gamma-function, following equations (6.1.1) and (6.2.1) in Press et al. (1992), where a is a positive real number.

Equipped with the probabilities for all the SFHs in the bootstrapping sample, we are able to modify the probability distribution of luminosity-weighted age and metallicity. In Fig. 14 we show the probability distribution obtained by convolving the integrated spectrum bootstrapping probability distribution function (Fig. 11) with the SBF spectrum probabilities.

Comparing the two distributions of luminosity-weighted ages and metallicities in Fig. 11 from the integrated spectrum and in Fig. 14 with the additional constraints from the SBF spectrum we find that both are similar.

For the other fits, we show the comparison of the two distributions (integrated spectrum bootstrapping and additional SBF constraints) in the appendix in Figs B2 for H β and B4 for H α with SPAA/MILES models and in Figs B6 for Hβ and B8 for Ca II with SPAA/Coelho models. The discrepancies in the ages and metallicities fitted in different wavelength regions are discussed in Section 7.3

7 DISCUSSION

7.1 Lessons learned about the models

Identifying and removing model uncertainties is important because many other conclusions are based on the results of stellar population synthesis predictions. We computed two model predictions with the same synthesis code, identical isochrones but different stellar spectral libraries. One is based on the observed stellar spectral library MILES (SPAA/MILES), and the other one is based on the theoretical stellar spectral library by Coelho (2014) (SPAA/Coelho). In the integrated spectra, the main differences are in the line strengths of the Balmer lines and the Fe I lines (see Figs 7 and 8 and Section 5.6).

The differences in the SBF spectra are more pronounced than in the integrated spectra. Figs 7 and 8 reveal that the molecular

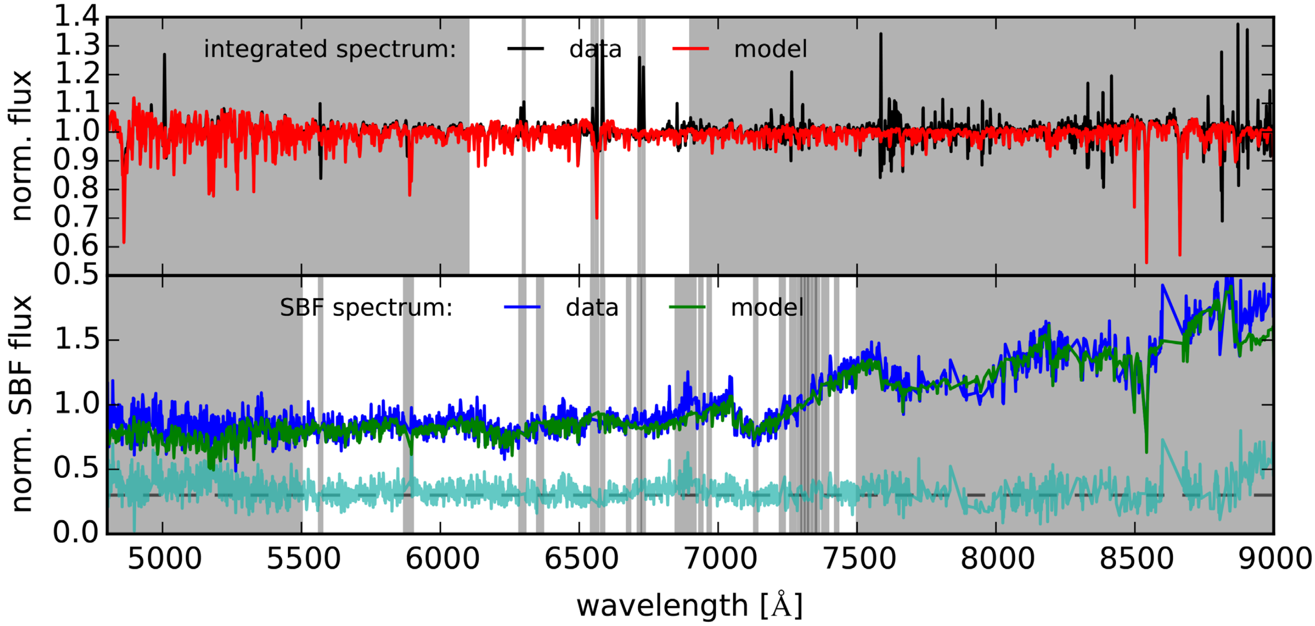

Figure 12. The SFH from the bootstrapping sample of the integrated spectrum with the best-fitting SBF model is compared to the NGC 5102 spectra. In the top panel, the integrated NGC 5102 spectrum is shown in black and the SPAA/Coelho integrated spectrum model in red. In the bottom panel, the NGC 5102 SBF spectrum is shown in blue and the SBF model spectrum in green. The residuals (SBF data − model) are shown in turquoise. Grey regions are masked during the fit/χ^2 computation.

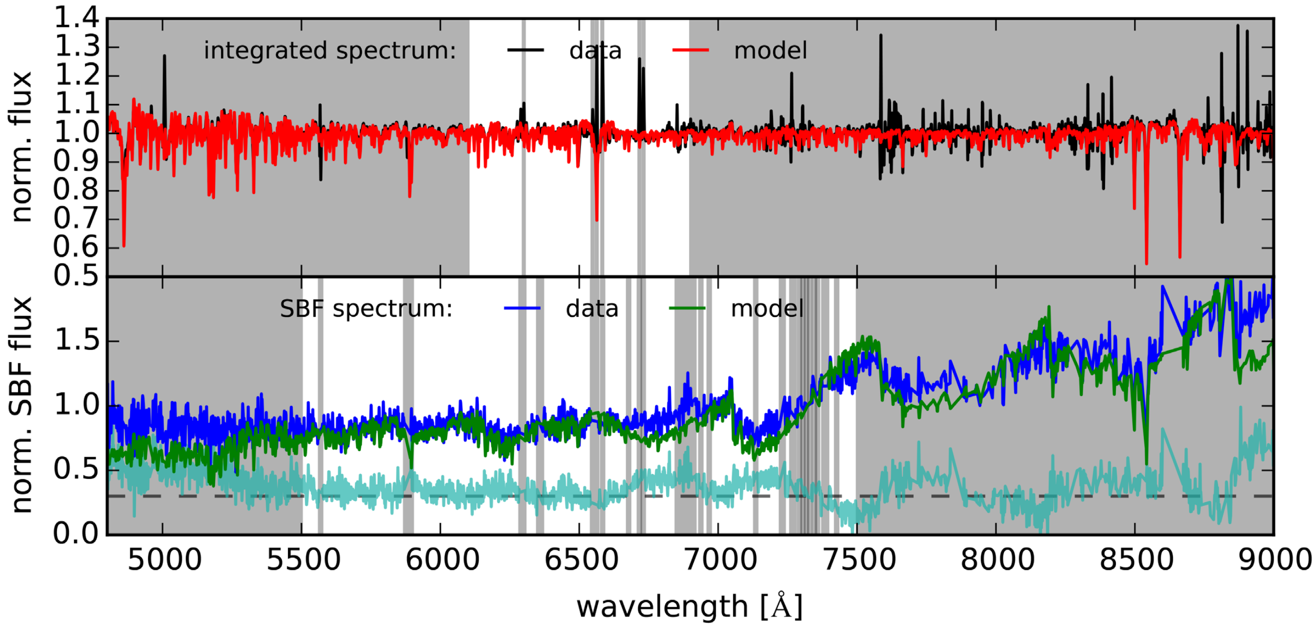

Figure 13. As Fig. 12, but for SFH from the bootstrapping sample of the integrated spectrum with the poorest fit of the SBF spectrum.

absorption bands are slightly stronger in the SPAA/Coelho models. Also, the evolution of the SBF spectra with age and metallicity is smoother in the SPAA/Coelho models than in the SPAA/MILES models. The comparison of the SPAA models to the NGC 5102 spectra does not favour one of the model sets over the other. Both sets of models (SPAA/MILES and SPAA/Coelho) can reproduce the observed NGC 5102 SBF spectrum.

The SBF spectrum of NGC 5102 is just a single observation of a single galaxy. In order to put stronger constraints on the models, we need more data from galaxies with other mean ages and metallicities. Good test cases for stellar population models are presented by GCs, as these are the objects with the simplest populations we know of. With MUSE, SBF spectra can be obtained for GCs in our Galaxy (where the available age range is strongly limited to old populations) and under good seeing conditions for some of the Large and Small Magellanic Cloud GCs, opening a wider age range. Especially the combination of crowded field spectroscopy (Kamann, Wisotzki & Roth 2013) and MUSE offers new possibilities: Applying crowded

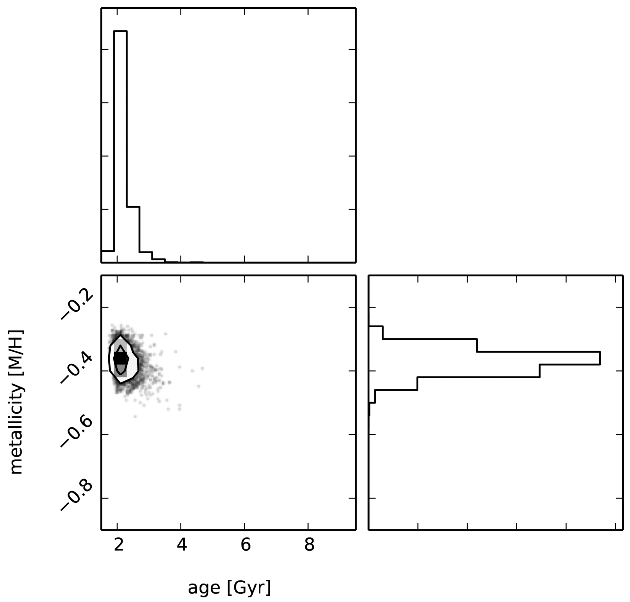

Figure 14. The distribution of luminosity-weighted ages and metallicities obtained by multiplying the results from bootstrapping the integrated spectrum in the H α region (Fig. 11) with the probabilities from SBF spectrum comparison. Every point represents one fit result in the bootstrapping sample. Grey shaded regions and contours are, however, probability densities, obtained by multiplying with the likelihood of representing the SBF spectrum. Contour lines are plotted at 0.5, 1.0, 1.5, and 2.0 σ.

field spectroscopy to MUSE data of the GC NGC 6397, Husser et al. (2016) have extracted spectra for more than 12 000 individual stars. Such a data set allows a direct comparison of isochrone properties, input spectra, integrated spectra, and SBF spectra. To our knowledge, such a test has never been done. Integrated GC spectra over a much broader range of ages and metallicities with good spectral resolution of 6800 and a large wavelength coverage are provided by the WAGGS project (Usher et al. 2017).

7.2 TP-AGB stars in the stellar population models

Stellar population models predict that SBFs are caused by giant stars (e.g. Liu et al. 2000) and the agreement of observed magnitudes and models supports this view. In this work, we show for the first time that the molecular features in the NGC 5102 SBF spectrum are very well reproduced by an M-type supergiant star spectrum. As discussed in Section 4, the number of carbon-rich stars expected at the metallicity of NGC 5102 is very low. In Appendix A, we demonstrate the sensitivity of the NGC 5102 SBF spectrum to a marginal contribution of C-type stars. This fit shows that in a statistical sense C-type stars are not needed to explain the NGC 5102 SBF spectrum.

In SPAA, isochrone points are connected to stellar spectra via a match in [Fe/H], T_{eff}, and log g. This means that the SPAA stellar population models do not include spectra from carbon-rich AGB stars. The reason is that in the observed MILES library no such stars are available and in the theoretical spectral library all stars have a solar-scaled composition, i.e. have oxygen-rich atmospheres. Due to the weak C-star contribution to the NGC 5102 SBF spectrum, this approximation does not influence our conclusions.

In order to fully exploit the potential of the SBF spectrum to constrain the AGB evolution, especially in more metal-poor galaxies, we would need population models that include stars with C-type spectra. The PARSEC isochrone predicts the C/O ratio, so this basic information is present. With the spectral libraries, the situation is a bit more complicated. In observational libraries, the AGB phase is typically not well covered over the full parameter range. There are dedicated TP-AGB libraries (Lançon & Mouhcine 2002) and the XSL includes a number of carbon stars (Chen et al. 2014; Gonneau et al. 2016, 2017), but the current DR1 sample does not provide enough spectra for stellar population synthesis modelling.

Theoretical stellar libraries provide typically solar-scaled and sometimes α-element-enhanced spectra, i.e. M-type spectra. The modelling of C-type stars is an active area of research (Aringer et al. 2009; Nowotny et al. 2011, 2013; Eriksson et al. 2014), so currently most theoretical libraries provide either oxygen- or carbon-rich spectra. There are, however, exceptions to this (e.g. Aringer et al. 2016), which are useful for stellar population synthesis modelling.

Another important aspect of AGB evolution is circumstellar dust that can strongly impact the optical spectra of individual stars (González-Lópezlira et al. 2010; Villaume, Conroy & Johnson 2015). Therefore, the inclusion of detailed TP-AGB spectra in the stellar population models goes beyond the scope of this work. All this emphasizes that there is significant room for improvement in stellar population models and that SBF spectra provide an additional way of constraining stellar population models, particularly with respect to the handling of AGB stars.

7.3 Dependence of the age and metallicity on central wavelength and stellar spectral library

We have used (when possible) three different wavelength regions (H β, H α, and Ca II-triplet) and two sets of models (SPAA/MILES and SPAA/Coelho) to fit the integrated spectrum and recover the SFH. In Fig. 15, we plot the mean luminosity-weighted ages and metallicities from the bootstrapping ensembles of the integrated spectrum fit. The plotted uncertainty intervals are the standard deviation of the bootstrapping ensemble.

There are two things worth mentioning. First, the different wavelength intervals that we used give different ages and metallicities. As PYPARADISE normalizes the observed spectrum and each template by the running mean, small changes in age and metallicity are to be expected. The differences that are visible in Fig. 15 are much larger and cannot be explained by continuum normalization. Whether or not the choice of wavelength interval used in the full spectrum fit biases the fit has not been investigated in depth. While Walcher et al. (2009) find that the wavelength range does influence the recovered ages and metallicities, Cezario et al. (2013) find that only ages are affected by the choice of the wavelength range.

The second point is that the two models predict different ages for the Hβ interval. This means that the models are not yet in agreement, especially as Hβ is an important age indicator.

The full spectrum fitting approach has been validated by different authors. The metallicities recovered by full spectrum fitting are usually found to be in agreement with colour-magnitude diagram studies (Koleva et al. 2008; Zhang et al. 2012; Ruiz-Lara et al. 2015; Kuncarayakti et al. 2016). The recovered ages of galactic GCs are sometimes found to be too young (Zhang et al. 2012); this is explained by the presence of a blue horizontal branch and blue straggler stars (Koleva et al. 2008; Ocvirk 2010) not included in the models. The results of the full spectrum fitting are dependent on the stellar library used, especially when complex star formation histories are included (Koleva et al. 2008; Chen et al. 2010; González Delgado & Cid Fernandes 2010).

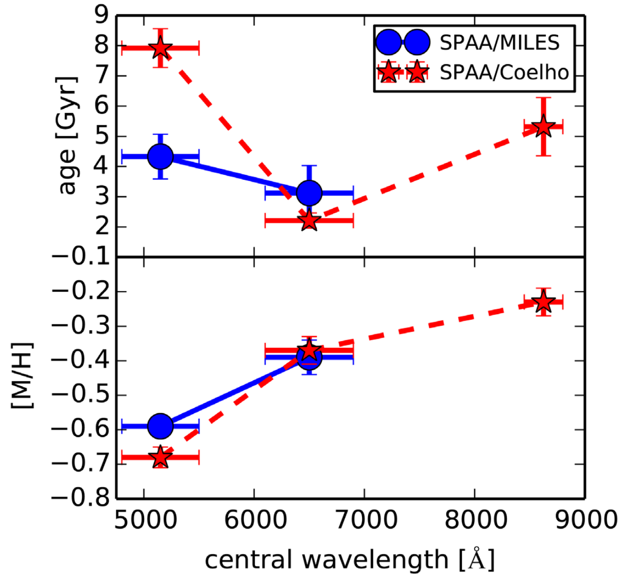

Figure 15. Luminosity-weighted ages (top) and metallicities (bottom) obtained by averaging the individual values in the bootstrapping sample of the integrated spectrum are shown. The fits where done with the two SSP libraries SPAA/MILES (blue dots, solid lines) and SPAA/Coelho (red stars, dashed lines) in up to three different wavelength intervals. Results are shown as a function of the central wavelength of the fitting interval; horizontal error bars show the width of the fit intervals. Vertical error bars are the 1σ standard deviations of the bootstrapping ensemble.

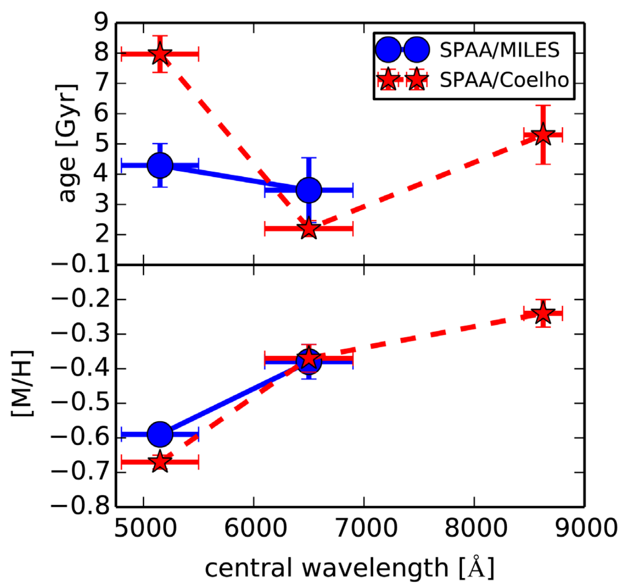

Figure 16. Luminosity-weighted ages and metallicities of the combined integrated and SBF spectrum fitting results are shown. Symbols are as in Fig. 15.

In Fig. 16, we plot the mean ages and metallicities obtained from the SFH distributions that include the additional constraints from the SBF fitting. The effect of including the SBF constraints on the mean ages and metallicities does not improve the situation.

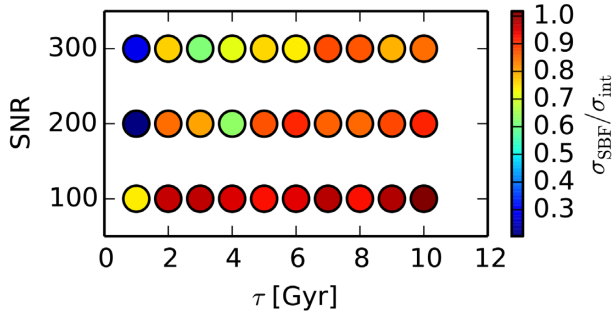

Figure 17. The reduction of uncertainties on the mean luminosity-weighted ages by using the additional SBF spectrum constraints is shown for a number of mock spectra. The colour code of the points gives the ratio of the width of age distribution from bootstrapping the integrated spectrum $\sigma_{\rm int}$ and after convolving this distribution with the probabilities from the SBF spectrum comparison $\sigma_{\rm SBF}$.

7.4 Constraining the SFH

In Section 6.2, we showed that different SFHs can represent the integrated spectrum similarly well but at the same time produce drastically different SBF model spectra. These additional constraints on the SFH lead, however, only to small reductions in the uncertainty of the mean luminosity-weighted ages and metallicities.

We investigated the question of whether we can expect the SBF spectrum to reduce the spread in the distribution of luminosity-weighted mean ages and metallicities. To answer this question, we created mock data by using the SPAA/MILES models and two different SFHs: single burst and so called τ-models, i.e. an exponentially declining SFH

$$\mathrm{SFH} \propto \exp(-t/\tau). \tag{19}$$

We added Gaussian noise to the mock data with zero mean and dispersion $\epsilon_{\rm int} = \langle F(\lambda)\rangle/\mathrm{SNR}$. We assumed that the noise on the SBF spectrum is a factor 10 higher $\epsilon_{\rm SBF} = 10\ \epsilon_{\rm int}$, roughly the factor we find in our data. We computed a grid of mock data for different ages/τ-values and SNRs and analysed them with the same code that we used to analyse the MUSE data.

We fitted the integrated mock spectrum with the approach detailed in Sections 6.1.1 and 6.1.2. The mean and the standard deviation σ in the luminosity-weighted ages and metallicities are computed from the 5000 bootstraps.

We compare the mock SBF spectrum to the bootstrapping results with the method that we described in Section 6.2. With the SBF constraints, we computed weighted mean ages and metallicities. In Fig. 17, we plot the ratio of $\sigma_{\rm SBF}/\sigma_{\rm int}$ (where σ is the width of the age distribution in the bootstrapping sample) for the τ-models. From this plot, we see that for an SNR $\sim$100 (i.e. SNR $\sim$10 in the SBF spectrum) the SBF spectrum decreases the uncertainty on mean luminosity-weighted ages only by 4 per cent (the median of $\sigma_{\rm SBF}/\sigma_{\rm int}$ is 0.96 at an SNR of 100). This is in very good agreement with the results from the MUSE spectra. We conclude that the analysis of the SBF spectrum constrains the full SFH, but does not give tighter constraints on mean ages and metallicities at the SNR values available here. However, we expect that for higher values of the SNR (of the integrated spectrum and the SBF spectrum) the SBF spectrum will further narrow down the distribution of ages.

We did an identical analysis with our mock spectra with SSP SFHs. This test leads to similar results and therefore we conclude that the relation between SNR and the reduction in mean age by using the additional SBF spectrum constraints is not strongly biased by the assumed SFH.

8 SUMMARY

We have for the first time applied the SBF method to integral field spectroscopy data. For this proof of concept study, we observed the galaxy NGC 5102 with the brightest *I*-band fluctuations, visible from the Paranal observatory during the science verification of the MUSE spectrograph.

We demonstrate that it is possible to apply the SBF method to MUSE data and to obtain SBF *spectra*. To our knowledge, this is the first SBF spectrum of a galaxy. The complex optics of the MUSE instrument lead to uncertainties in the sky subtraction that, in the presence of sky lines, result in fluctuations that outshine the stellar fluctuations at some wavelengths. We masked those wavelength regions.

The comparison of the SBF spectrum with *stellar spectra* reveals that M-type giant stars are the major contributors to the SBF signal of NGC 5102. The SBF spectrum is the luminosity-weighted average flux and as such represents at every wavelength the flux of a typical giant star (e.g. Tonry, Ajhar & Luppino 1990).

We developed the stellar population synthesis code SPAA that predicts SBF spectra. We have computed SPAA stellar population models based on observed and theoretical stellar spectra. We show that the single-burst integrated spectra agree well with published SSP spectra.

The SBF spectra reveal that the SPAA models based on theoretical spectra predict stronger molecular features. These differences between the population models are hardly seen in the integrated spectrum. This reveals the potential of SBF spectra for highlighting differences in stellar population models. The NGC 5102 SBF spectrum can be represented well by both sets of models. To further differentiate between the two sets of models, we need data for more galaxies, especially over a range of metallicities and ages.

We fitted the SFH of NGC 5102 in three different wavelength regions and with both of our model sets. The inferred star formation histories typically agree between the two sets of models. However, different wavelength intervals lead to strongly differing mean ages and metallicities. As discussed, the differing SFHs obtained in different wavelength intervals need to be investigated to understand which spectral region is best suited for population studies.

The SBF spectrum does provide valuable additional constraints on the SFH. These constraints lead, however, only to marginal reductions in the uncertainty of mean luminosity-weighted ages and metallicities. With mock data, we show that this is to be expected.

ACKNOWLEDGEMENTS

We thank the anonymous referee for thoroughly reading the paper and for comments that improved its quality. We thank Oliver Rieger for his contributions to coding the SPAA software. We thank Charlie Conroy for his comments on an earlier version of the manuscript. MM is grateful for financial support from the Leibniz Graduate School for Quantitative Spectroscopy in Astrophysics, a joint project of the Leibniz Institute for Astrophysics Potsdam (AIP) and the Institute of Physics and Astronomy of the University of Potsdam (UP). M-RLC acknowledges support from the European Research Council (ERC) under the European Union's Horizon 2020 research and innovation programme (grant agreement No 682115). This work is based on observations collected at the European Organisation for Astronomical Research in the Southern Hemisphere under ESO programme 60.A-9308(A).

REFERENCES

Ajhar E. A., Tonry J. L., 1994, ApJ, 429, 557
Alonso A., Arribas S., Martinez-Roger C., 1996, A&A, 313, 873
Alonso A., Arribas S., Martínez-Roger C., 1999, A&AS, 140, 261
Aringer B., Girardi L., Nowotny W., Marigo P., Bressan A., 2016, MNRAS, 457, 3611
Aringer B., Girardi L., Nowotny W., Marigo P., Lederer M. T., 2009, A&A, 503, 913
Bacon R. et al., 2010, in McLean I. S., Ramsay S. K., Takami H., eds, SPIE Conf. Ser. Vol. 7735, Ground-based and Airborne Instrumentation for Astronomy III. SPIE, Bellingham, p. 773508
Battinelli P., Demers S., 2005, A&A, 434, 657
Beaulieu S. F., Freeman K. C., Hidalgo S. L., Norman C. A., Quinn P. J., 2010, AJ, 139, 984
Beifiori A., Maraston C., Thomas D., Johansson J., 2011, A&A, 531, A109
Biscardi I., Raimondo G., Cantiello M., Brocato E., 2008, ApJ, 678, 168
Blakeslee J. P. et al., 2009, ApJ, 694, 556
Bressan A., Marigo P., Girardi L., Salasnich B., Dal Cero C., Rubele S., Nanni A., 2012, MNRAS, 427, 127
Bruzual G., Charlot S., 2003, MNRAS, 344, 1000
Caffau E., Ludwig H.-G., Steffen M., Freytag B., Bonifacio P., 2011, Sol. Phys., 268, 255
Cantiello M., Blakeslee J., Raimondo G., Brocato E., Capaccioli M., 2007, ApJ, 668, 130
Cantiello M., Raimondo G., Brocato E., Capaccioli M., 2003, AJ, 125, 2783
Cappellari M., Copin Y., 2003, MNRAS, 342, 345
Cappellari M., Emsellem E., 2004, PASP, 116, 138
Carretta E., Gratton R. G., 1997, A&AS, 121
Cenarro A. J., Gorgas J., Cardiel N., Pedraz S., Peletier R. F., Vazdekis A., 2001, MNRAS, 326, 981
Cenarro A. J. et al., 2007, MNRAS, 374, 664
Cezario E., Coelho P. R. T., Alves-Brito A., Forbes D. A., Brodie J. P., 2013, A&A, 549, A60
Chabrier G., 2003, PASP, 115, 763
Charlot S., Bruzual A. G., 1991, ApJ, 367, 126
Chen X. Y., Liang Y. C., Hammer F., Prugniel P., Zhong G. H., Rodrigues M., Zhao Y. H., Flores H., 2010, A&A, 515, A101
Chen Y., 2013, PhD thesis, University of Groningen
Chen Y.-P., Trager S. C., Peletier R. F., Lançon A., Vazdekis A., Prugniel P., Silva D. R., Gonneau A., 2014, A&A, 565, A117
Cioni M.-R. L., 2009, A&A, 506, 1137
Cioni M.-R. L., Habing H. J., 2003, A&A, 402, 133
Coelho P., Bruzual G., Charlot S., Weiss A., Barbuy B., Ferguson J. W., 2007, MNRAS, 382, 498
Coelho P. R. T., 2014, MNRAS, 440, 1027
Conroy C., Gunn J. E., White M., 2009, ApJ, 699, 486
Davidge T. J., 2008, AJ, 135, 1636
Davidge T. J., 2015, ApJ, 799, 97
Deharveng J.-M., Jedrzejewski R., Crane P., Disney M. J., Rocca-Volmerange B., 1997, A&A, 326, 528
Dunn L. P., Jerjen H., 2006, AJ, 132, 1384
Eggen O. J., 1971, QJRAS, 12, 305
Eminian C., Kauffmann G., Charlot S., Wild V., Bruzual G., Rettura A., Loveday J., 2008, MNRAS, 384, 930
Eriksson K., Nowotny W., Höfner S., Aringer B., Wachter A., 2014, A&A, 566, A95
Falcón-Barroso J., Sánchez-Blázquez P., Vazdekis A., Ricciardelli E., Cardiel N., Cenarro A. J., Gorgas J., Peletier R. F., 2011, A&A, 532, A95
Feast M. W., Abedigamba O. P., Whitelock P. A., 2010, MNRAS, 408, L76
Fruchter A., Sosey M., Hack W., Dressel L., Koekemoer A. M., Mack J., Mutchler M., Pirzkal N., 2009, The MultiDrizzle Handbook, Space Telescope Science Institute, Baltimore, Maryland, US

Fu X., Bressan A., Marigo P., Girardi L., Montalbán J., Chen Y., Nanni A., 2018, MNRAS, 476, 496
Gallagher J. S., Faber S. M., Balick B., 1975, ApJ, 202, 7
Gallart C., Zoccali M., Aparicio A., 2005, ARA&A, 43, 387
Girardi L., Bressan A., Bertelli G., Chiosi C., 2000, A&AS, 141, 371
Gonneau A. et al., 2016, A&A, 589, A36
Gonneau A. et al., 2017, A&A, 601, A141
González-Lópezlira R. A., Bruzual-A. G., Charlot S., Ballesteros-Paredes J., Loinard L., 2010, MNRAS, 403, 1213
González Delgado R. M., Cid Fernandes R., 2010, MNRAS, 403, 797
Greene J. E., Murphy J. D., Graves G. J., Gunn J. E., Raskutti S., Comerford J. M., Gebhardt K., 2013, ApJ, 776, 64
Grevesse N., Sauval A. J., 1998, Space Sci. Rev., 85, 161
Gustafsson B., Edvardsson B., Eriksson K., Jørgensen U. G., Nordlund Å., Plez B., 2008, A&A, 486, 951
Hamren K. et al., 2016, ApJ, 828, 15
Hamren K. M. et al., 2015, ApJ, 810, 60
Herwig F., 2005, ARA&A, 43, 435
Husemann B., Bennert V. N., Scharwächter J., Woo J.-H., Choudhury O. S., 2016, MNRAS, 455, 1905
Husser T.-O., Wende-von Berg S., Dreizler S., Homeier D., Reiners A., Barman T., Hauschildt P. H., 2013, A&A, 553, A6
Husser T.-O. et al., 2016, A&A, 588, A148
Jensen J. B., Blakeslee J. P., Gibson Z., Lee H.-c., Cantiello M., Raimondo G., Boyer N., Cho H., 2015, ApJ, 808, 91
Jensen J. B., Tonry J. L., Luppino G. A., 1998, ApJ, 505, 111
Jensen J. B., Tonry J. L., Thompson R. I., Ajhar E. A., Lauer T. R., Rieke M. J., Postman M., Liu M. C., 2001, ApJ, 550, 503
Kacharov N., Rejkuba M., Cioni M.-R. L., 2012, A&A, 537, A108
Kamann S., Wisotzki L., Roth M. M., 2013, A&A, 549, A71
Kamphuis P., Józsa G. I. G., Oh S.-. H., Spekkens K., Urbancic N., Serra P., Koribalski B. S., Dettmar R.-J., 2015, MNRAS, 452, 3139
Karachentsev I. D. et al., 2002, A&A, 385, 21
Koleva M., Prugniel P., Ocvirk P., Le Borgne D., Soubiran C., 2008, MNRAS, 385, 1998
Krajnović D. et al., 2011, MNRAS, 414, 2923
Kroupa P., 2001, MNRAS, 322, 231
Kuncarayakti H., Galbany L., Anderson J. P., Krühler T., Hamuy M., 2016, A&A, 593, A78
Kurucz R. L., 1970, SAO Special Report, 309
Kurucz R. L., Avrett E. H., 1981, SAO Special Report, 391
Lançon A., Mouhcine M., 2002, A&A, 393, 167
Le Borgne D., Rocca-Volmerange B., Prugniel P., Lançon A., Fioc M., Soubiran C., 2004, A&A, 425, 881
Leitherer C. et al., 1999, ApJS, 123, 3
Liu M. C., Charlot S., Graham J. R., 2000, ApJ, 543, 644
Liu M. C., Graham J. R., Charlot S., 2002, ApJ, 564, 216
Maraston C., 2005, MNRAS, 362, 799
Marigo P., Bressan A., Nanni A., Girardi L., Pumo M. L., 2013, MNRAS, 434, 488
Marigo P. et al., 2017, ApJ, 835, 77
McMillan R., Ciardullo R., Jacoby G. H., 1994, AJ, 108, 1610
Mei S. et al., 2005, ApJS, 156, 113
Mitzkus M., Cappellari M., Walcher C. J., 2017, MNRAS, 464, 4789
Mollá M., García-Vargas M. L., Bressan A., 2009, MNRAS, 398, 451
Nowotny W., Aringer B., Höfner S., Eriksson K., 2013, A&A, 552, A20
Nowotny W., Aringer B., Höfner S., Lederer M. T., 2011, A&A, 529, A129
Ocvirk P., 2010, ApJ, 709, 88
Pahre M. A., Mould J. R., 1994, ApJ, 433, 567
Pahre M. A. et al., 1999, ApJ, 515, 79
Pietrinferni A., Cassisi S., Salaris M., Castelli F., 2004, ApJ, 612, 168
Press W. H., Teukolsky S. A., Vetterling W. T., Flannery B. P., 1992, Numerical Recipes in C: The Art of Scientific Computing, 2nd edn. Cambridge Univ. Press, Cambridge
Pritchet C., 1979, ApJ, 231, 354
Prugniel P., Soubiran C., 2001, A&A, 369, 1048
Prugniel P., Vauglin I., Koleva M., 2011, A&A, 531, A165
Raimondo G., 2009, ApJ, 700, 1247
Raimondo G., Brocato E., Cantiello M., Capaccioli M., 2005, AJ, 130, 2625
Rosenfield P., Marigo P., Girardi L., Dalcanton J. J., Bressan A., Williams B. F., Dolphin A., 2016, ApJ, 822, 73
Roth M.M., et al., 2018, A&A, in press
Ruiz-Lara T. et al., 2015, A&A, 583, A60
Sbordone L., Bonifacio P., Castelli F., Kurucz R. L., 2004, Memorie della Societa Astronomica Italiana Supplementi, 5, 93
Scheuer P. A. G., 1957, Proc. Camb. Phil. Soc., 53, 764
Sodemann M., Thomsen B., 1996, AJ, 111, 208
Sánchez-Blázquez P. et al., 2006, MNRAS, 371, 703
Taylor E. N. et al., 2011, MNRAS, 418, 1587
Tonry J., Schneider D. P., 1988, AJ, 96, 807
Tonry J. L., 1991, ApJ, 373, L1
Tonry J. L., Ajhar E. A., Luppino G. A., 1990, AJ, 100, 1416
Tonry J. L., Blakeslee J. P., Ajhar E. A., Dressler A., 1997, ApJ, 475, 399
Tonry J. L., Dressler A., Blakeslee J. P., Ajhar E. A., Fletcher A. B., Luppino G. A., Metzger M. R., Moore C. B., 2001, ApJ, 546, 681
Trager S. C., Faber S. M., Worthey G., González J. J., 2000a, AJ, 119, 1645
Trager S. C., Faber S. M., Worthey G., González J. J., 2000b, AJ, 120, 165
Tully R. B., Libeskind N. I., Karachentsev I. D., Karachentseva V. E., Rizzi L., Shaya E. J., 2015, ApJ, 802, L25
Usher C. et al., 2017, MNRAS, 468, 3828
van den Bergh S., 1976, AJ, 81, 795
van den Bosch R. C. E., van de Ven G., 2009, MNRAS, 398, 1117
van Dokkum P. G., Conroy C., 2014, ApJ, 797, 56
van Woerden H., van Driel W., Braun R., Rots A. H., 1993, A&A, 269, 15
Vazdekis A., Ricciardelli E., Cenarro A. J., Rivero-González J. G., Díaz-García L. A., Falcón-Barroso J., 2012, MNRAS, 424, 157
Vazdekis A., Sánchez-Blázquez P., Falcón-Barroso J., Cenarro A. J., Beasley M. A., Cardiel N., Gorgas J., Peletier R. F., 2010, MNRAS, 404, 1639
Villaume A., Conroy C., Johnson B. D., 2015, ApJ, 806, 82
Walcher C. J., Coelho P., Gallazzi A., Charlot S., 2009, MNRAS, 398, L44
Walcher C. J., Coelho P. R. T., Gallazzi A., Bruzual G., Charlot S., Chiappini C., 2015, A&A, 582, A46
Weilbacher P. M., Streicher O., Urrutia T., Jarno A., Pécontal-Rousset A., Bacon R., Böhm P., 2012, in Radziwill N. M., Chiozzi G., eds, SPIE Conf. Ser. Vol. 8451, Software and Cyberinfrastructure for Astronomy II. SPIE, Bellingham, p. 84510B
Worthey G., 1993, ApJ, 409, 530
Worthey G., Faber S. M., Gonzalez J. J., 1992, ApJ, 398, 69
Zhang Y., Han Z., Liu J., Zhang F., Kang X., 2012, MNRAS, 421, 1678
Zhu G., Blanton M. R., Moustakas J., 2010, ApJ, 722, 491
Zibetti S., Charlot S., Rix H.-W., 2009, MNRAS, 400, 1181

APPENDIX A: CARBON STAR FEATURES IN THE SBF SPECTRUM

In Section 4, we showed that the SBF spectrum is well represented by an M-type stellar spectrum. Carbon stars might, however, contribute to the SBF spectrum of NGC 5102 and we test this here.

The best-fitting spectrum from the carbon-related XSL spectra is the only S-type spectrum (S-type stars have equal amounts of carbon and oxygen in their atmospheres), where C/O = 1.0. This again confirms that stars with oxygen-rich atmospheres reproduce the SBF spectrum better. In Fig. A1, we instead show one of the best-fitting C-type spectra, to emphasize the difference compared to the M-type spectrum. It is immediately obvious that the C-type spectrum provides a much poorer fit to the SBF spectrum than the M-type spectrum in Fig. 4. Some of the features that are not well represented by the M-type spectrum have corresponding features in the C-type stellar spectrum.

We therefore fitted a linear combination of the best-fitting M-type spectrum and a well-fitting C-type spectrum to the SBF spectrum. In a χ^2 sense, this fit is only a marginal improvement over the M-type spectrum fit. This means that statistically a C-type spectrum is not

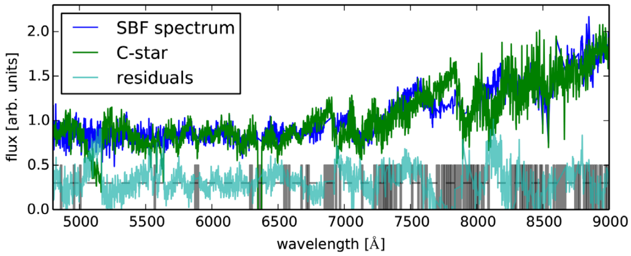

Figure A1. The SBF spectrum of NGC 5102 is shown in blue. One of the best-fitting C-type spectra from the XSL library (green) is compared to the SBF spectrum. The residuals (SBF − C-type spectrum) are shown in turquoise. This plot shows that the SBF spectrum of NGC 5102 is not dominated by C-type stars. Some lines in the region between 7600 and 7900 Å are reminiscent of features in C-type star spectra. Grey regions are masked sky and emission lines and regions where the XSL spectrum is missing.

needed to explain the SBF spectrum of NGC 5102. However, if we assume that there must be C-stars in NGC 5102, then the SBF spectrum allows for about 5 per cent luminosity-weighted contribution of those stars. This highlights the sensitivity of the SBF spectrum to an extremely small fraction of carbon stars.

The luminosity-weighted contribution of C-type stars cannot be directly compared to the number count ratios, especially as this involves the intrinsic brightness of M- and C-type stars as well as distinguishing M-type stars on the RGB and AGB (Hamren et al. 2015, 2016). With MUSE, it has even become possible under excellent seeing conditions to resolve the nearby galaxy NGC 300 into stars and directly determine the C/M ratio from individual stars with high-quality spectra (Roth et al. 2018). In order to get a better understanding of the C-star population, it would be extremely useful to obtain an SBF spectrum in the near-infrared, where the dust obscuration is much less of an issue.

APPENDIX B: HISTOGRAMS FOR OTHER WAVELENGTH REGIONS AND MODELS

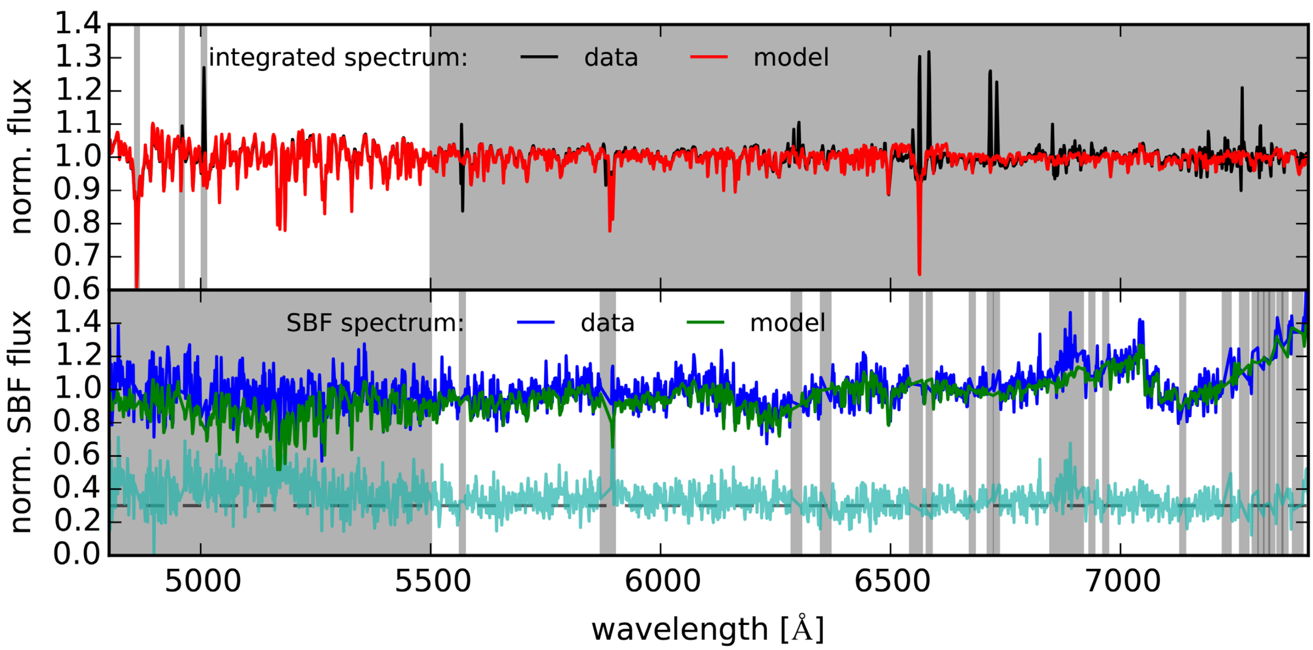

Figure B1. The SFH from the bootstrapping sample of the Hβ interval, fitted with SPAA/MILES models, with the best-fitting SBF model compared to the NGC 5102 spectrum. In the top panel, the integrated NGC 5102 spectrum is shown in black and the SPAA/MILES integrated spectrum model in red. In the bottom panel, the NGC 5102 SBF spectrum is shown in blue and the SBF model spectrum in green. The residuals (SBF data − model) are shown in turquoise. Grey regions are masked during the fit/χ^2 computation.

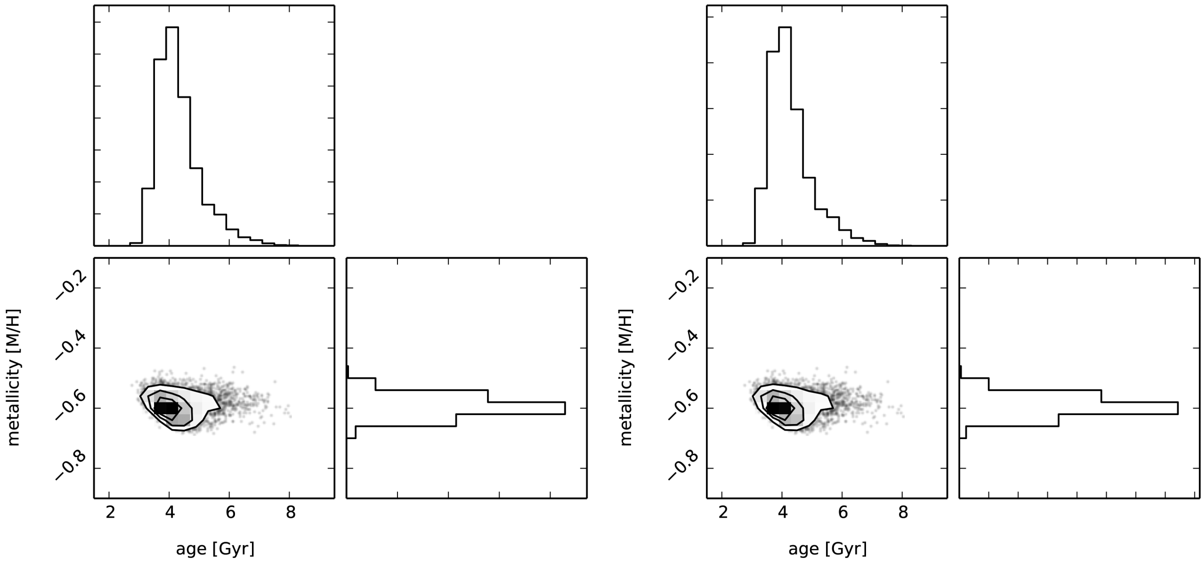

Figure B2. Left: The distribution of luminosity-weighted ages and metallicities obtained by fitting the Hβ wavelength region with SPAA/MILES models. Every point represents the average luminosity-weighted quantities of a non-parametric SFH fit. In the densest regions, the density of points is represented by grey-scale values. Right: The distribution of luminosity-weighted ages and metallicities obtained by folding the distribution in the left panel with the probabilities from SBF spectrum comparison. Every point represents one fit result in the bootstrapping sample. Grey shaded regions and contours are, however, probability densities, obtained by folding with the likelihood of representing the SBF spectrum. Contour lines are plotted at 0.5, 1.0, 1.5, and 2.0 σ.

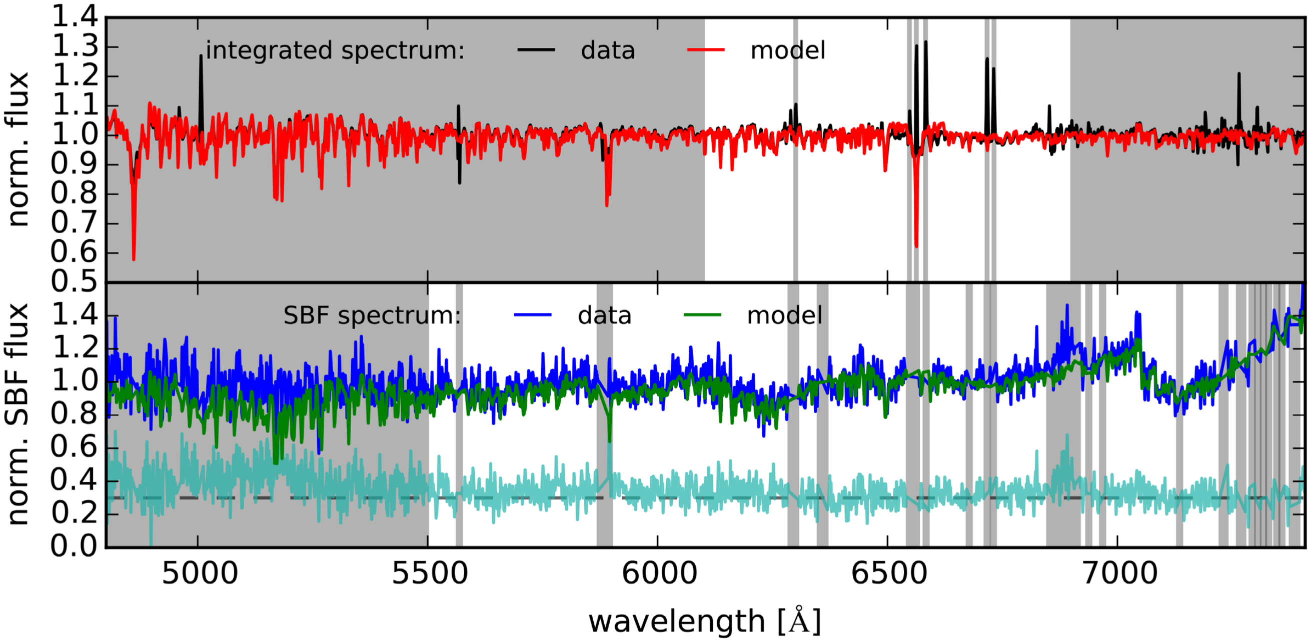

Figure B3. The SFH from the bootstrapping sample of the H α interval, fitted with SPAA/MILES models, with the best-fitting SBF model compared to the NGC 5102 spectrum. Panels as in Fig. B1.

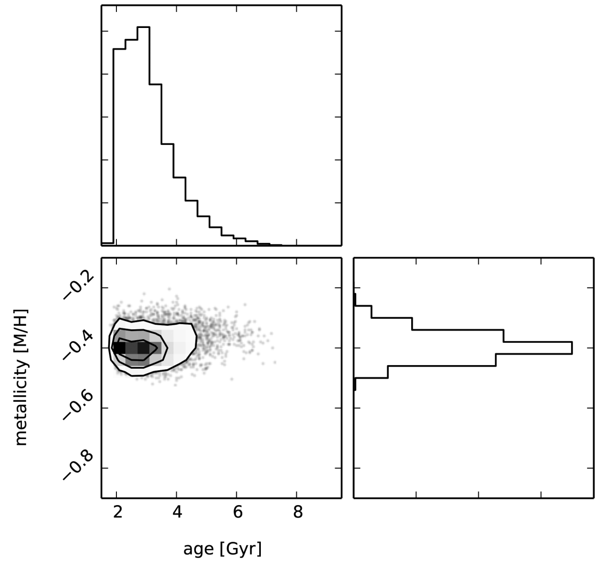

Figure B4. Like Fig. B2 but for the H α wavelength region fitted with SPAA/MILES models.

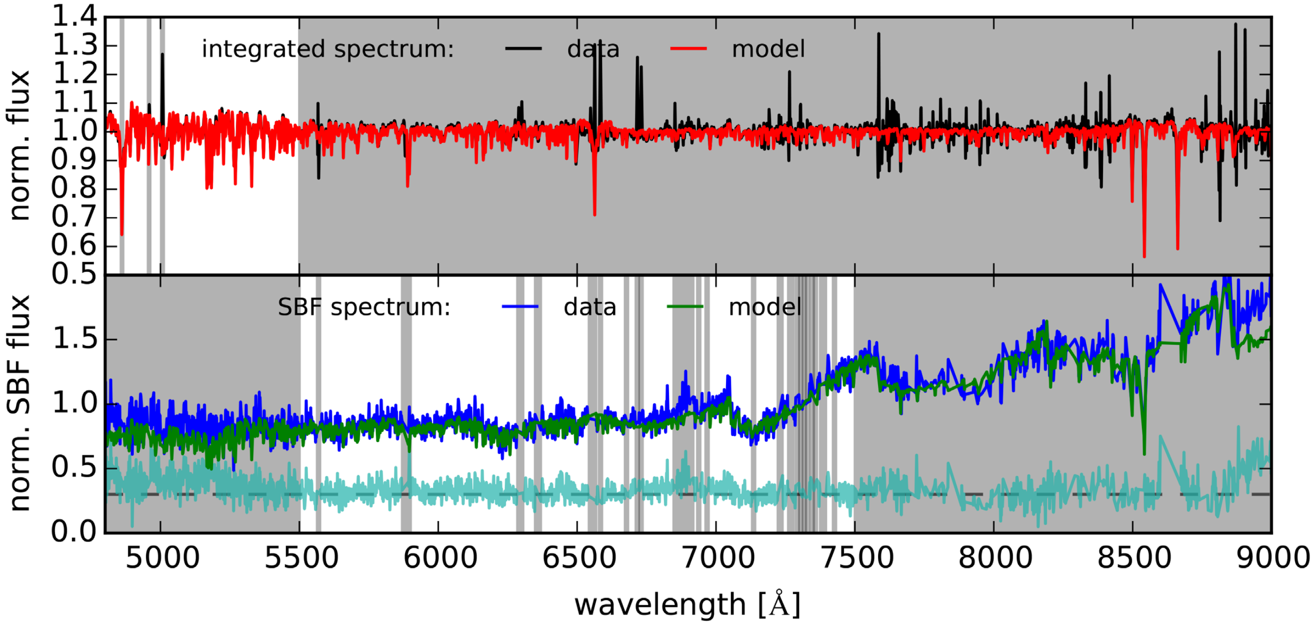

Figure B5. The SFH from the bootstrapping sample of the Hβ interval, fitted with SPAA/Coelho models, with the best-fitting SBF model compared to the NGC 5102 spectrum. Panels as in Fig. B1.

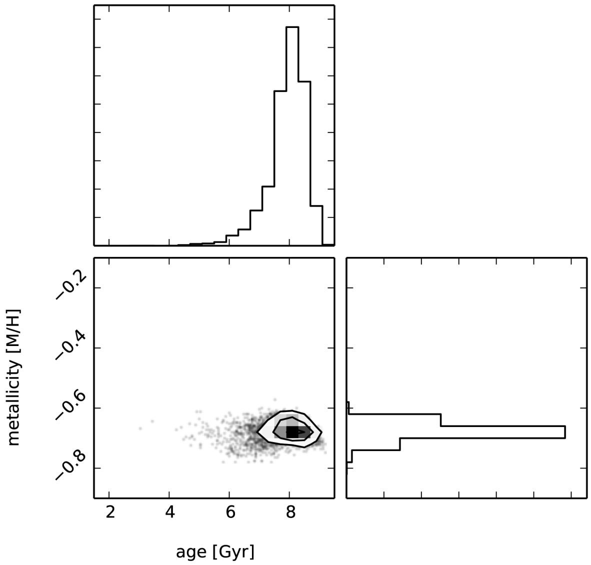

Figure B6. Like Fig. B2 but for the H β wavelength region fitted with SPAA/Coelho models.

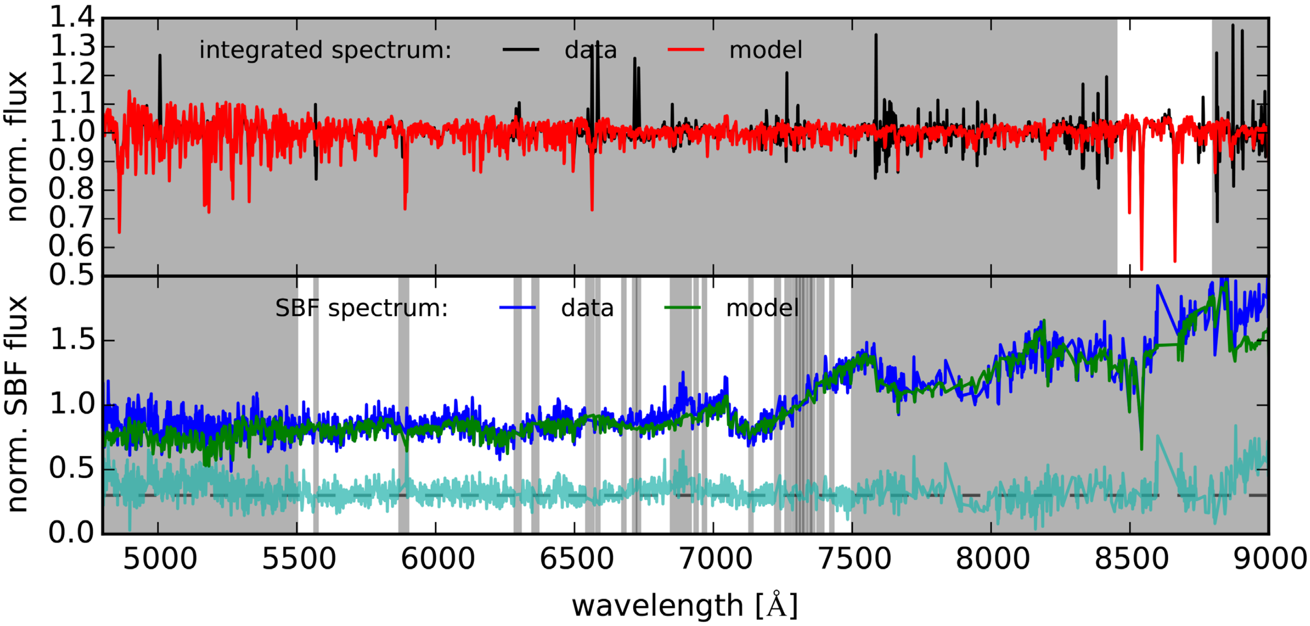

Figure B7. The SFH from the bootstrapping sample of the Ca II interval, fitted with SPAA/Coelho models, with the best-fitting SBF model compared to the NGC 5102 spectrum. Panels as in Fig. B1.

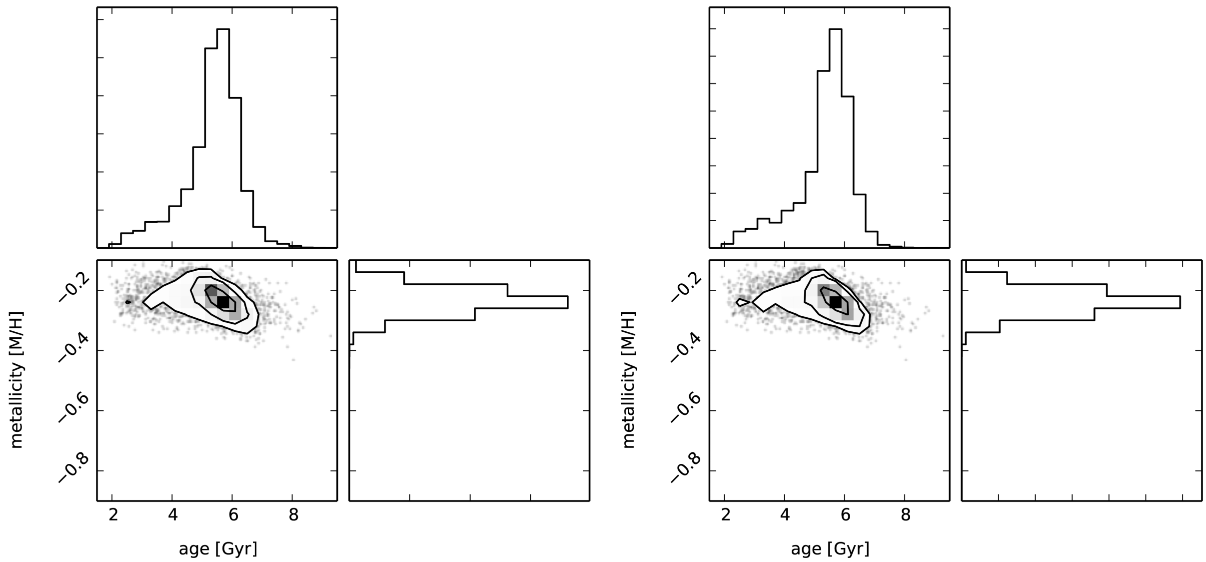

Figure B8. Like Fig. B2 but for the Ca II-triplet wavelength region fitted with SPAA/Coelho models.

This paper has been typeset from a TEX/LATEX file prepared by the author.